AGU ADVANCING EARTH AND SPACE SCIENCES

Geochemistry, Geophysics, Geosystems®

RESEARCH ARTICLE
10.1029/2023GC011340

Effect of Water-Rock Ratio on the Stable Isotope Record of Fluid-Rock-Deformation Interactions in Detachment Shear Zone

Raphaël Gottardi[1,2], **Camron Mire**[2], **Niya Davis**[2], **and Gabriele Casale**[3]

[1]Department of Geosciences, Auburn University, Auburn, AL, USA, [2]School of Geosciences, University of Louisiana at Lafayette, Lafayette, LA, USA, [3]Department of Geological and Environmental Sciences, Appalachian State University, Boone, NC, USA

Key Points:

- Hydrogen isotope analyses revealed that the fluid that filled and precipitated in the quartz veins was meteoric in origin
- Differences in stable isotope depletion correlate with muscovite content, which may be related to the original porosity of the mylonite
- Fluid-rock ratio depletion modeling suggests that the DSZ was rock-dominated with the highest fluid-rock ratio of ~0.1

Correspondence to:
R. Gottardi,
gottardi@auburn.edu

Citation:
Gottardi, R., Mire, C., Davis, N., & Casale, G. (2024). Effect of water-rock ratio on the stable isotope record of fluid-rock-deformation interactions in detachment shear zone. *Geochemistry, Geophysics, Geosystems*, *25*, e2023GC011340. https://doi.org/10.1029/2023GC011340

Received 13 NOV 2023
Accepted 25 MAR 2024

Author Contributions:
Conceptualization: Raphaël Gottardi
Data curation: Raphaël Gottardi
Formal analysis: Raphaël Gottardi, Camron Mire, Niya Davis
Funding acquisition: Raphaël Gottardi
Investigation: Raphaël Gottardi, Camron Mire, Niya Davis
Methodology: Raphaël Gottardi
Project administration: Raphaël Gottardi
Resources: Raphaël Gottardi
Supervision: Raphaël Gottardi
Validation: Raphaël Gottardi
Visualization: Raphaël Gottardi
Writing – original draft: Raphaël Gottardi, Camron Mire
Writing – review & editing: Raphaël Gottardi, Gabriele Casale

Abstract

Oxygen and hydrogen stable isotope analyses of quartz and muscovite veins from the footwall of the Raft River detachment shear zone (Utah) provide insight into the hydrology and fluid-rock interactions during ductile deformation. Samples were collected from veins containing 90%–100% quartz with orientations either at a high angle or sub-parallel to the surrounding quartzite mylonite foliation. Stable isotope analysis was performed on 10 samples and compared with previous quartzite mylonite isotope data sets. The results indicate that the fluid present during deformation of the shear zone was meteoric in origin, with a δ^2H value of approximately −100‰ and a δ^{18}O value of approximately −13.7‰. Oxygen stable isotope O^{18}O depletion correlates with the muscovite content of the analyzed rocks. Many of the analyzed samples in this and other studies show an apparent lack of equilibrium between the oxygen and hydrogen isotope systems, which can be explained by hydrogen and oxygen isotope exchange at varying fluid-rock ratios. Our results suggest that the Raft River detachment shear zone had a low static fluid-rock ratio (<0.1), yet experienced episodic influxes of fluids through semi-brittle structures. This fluid was then expelled out into the surrounding mylonite following progressive shearing, causing further ^{18}O-depletion and fluid-related embrittlement.

1. Introduction

Fluids play a major role in rock deformation and failure processes, especially under high temperature and stress conditions found in mid- to lower-crustal detachment shear zones (DSZs, e.g., Gottardi & Hughes, 2022; Menegon et al., 2015; Spruzeniece & Piazolo, 2015; Stenvall et al., 2020; Wehrens et al., 2016). Fluids weaken rocks under stress through multiple physio-chemical mechanisms, such as pressure-solution creep (e.g., Gratier et al., 2013; Shimizu, 1995; Wassmann & Stőckhert, 2013), hydrolytic weakening (e.g., Griggs, 1967; Kronenberg & Tullis, 1984; Okazaki et al., 2021; Pongrac et al., 2022; Stünitz et al., 2017), metamorphic reactions and mass transport (e.g., Carter et al., 1990; Ferry, 1994; Hobbs et al., 2010; Labrousse et al., 2010; Whyte et al., 2021), causing departure from experimentally derived failure laws (Figure 1).

The strength of the lithosphere is classically described by two empirically derived constitutive equations: the Coulomb frictional failure for the upper crust and ductile flow laws for the lower crust. In this model, the rheology of the cool, brittle upper crust follows Byerlee's law, which predicts a linear increase in strength with depth (Byerlee, 1978; Figure 1). As depth increases, elevated temperature favors crystal plasticity and dynamic recrystallization, and rocks eventually deform ductilely. Ductile behavior is modeled by flow laws that are functions of differential stress, strain rate, temperature, grain size, fluid activity, and deformation mechanisms of the rheologically significant mineral species (Brace & Kohlstedt, 1980; Kusznir & Park, 1987). However, there is an apparent discrepancy between the strength predicted by failure laws derived largely from deformation experiments, and rheological and mechanical studies of fault and shear zones: field studies demonstrate that fault and shear zones are much weaker than described by either criterion (e.g., Behr & Platt, 2014 and references therein). This rheological weakening in naturally deformed rocks is attributed to the aforementioned fluid-driven weakening mechanisms.

Because fluid-related processes have such a strong weakening effect on the strength of the lithosphere, it is therefore critical to understand fluid migration pathways and fluid-rock-deformation mechanisms. DSZs associated with metamorphic core complexes provide excellent exposure of mid- to lower crustal rocks to study such processes (e.g., Fricke et al., 1992; Gébelin et al., 2011, 2015; Gottardi & Hughes, 2022; Gottardi et al., 2011,

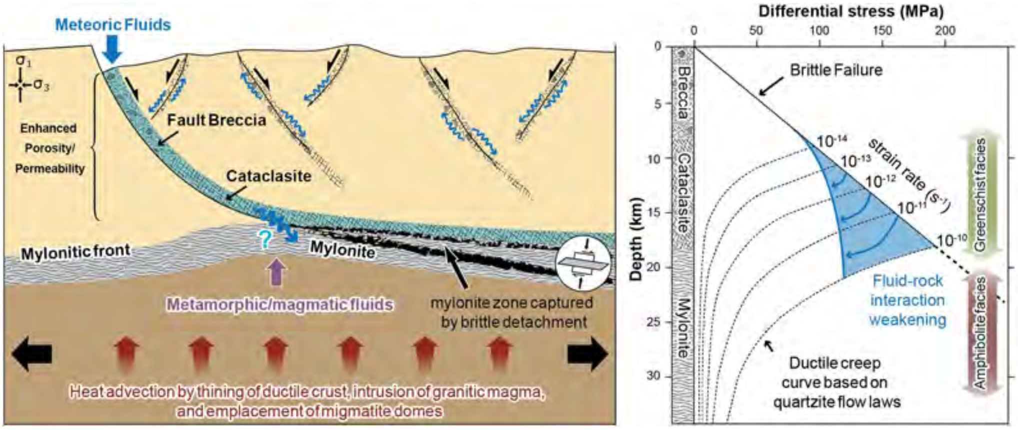

Figure 1. Fluid-rock-deformation interaction in a detachment shear zone (modified from Gottardi and Hughes (2022)).

2015, 2018; Morrison & Anderson, 1998; Mulch et al., 2007; Quilichini et al., 2015, 2016). Since DSZs evolve at the brittle-ductile transition (e.g., Behr & Platt, 2014), they provide a unique opportunity to investigate how fluids permeate from the brittle upper crust to the ductile lower crust. In the upper crust, fluid flow is controlled by brittle faulting and fracturing, which typically increases the porosity and permeability of the rock (e.g., McCaig, 1988; Sibson, 1992; Wehrens et al., 2016). Faults have been shown to exhibit fault-valve behavior or "seismic pumping," becoming highly permeable after seismic failure and channeling fluid discharge in the seismogenic zone (Sibson, 1990, 1992). However, in the ductile regime, where rocks can heal and recrystallize, the mechanisms of fluid penetration and circulation are conceptually challenging (e.g., Connolly & Podladchikov, 2004), although some studies have shown that porosity may increase through high temperature plastic deformation (Gilgannon et al., 2020), and creep cavitation (Fusseis et al., 2009; Menegon et al., 2015).

At high temperatures, fluid-rock interactions can be investigated using stable isotope geochemistry (e.g., Baumgartner & Valley, 2001; Valley, 2001). Based on oxygen and hydrogen stable isotope geochemistry combined with argon geochronology, syn-kinematic fluids in DSZs have been attributed to a variety of sources, including meteoric water (Bons & Gomez-Rivas, 2020; Dusséaux et al., 2022; Fricke et al., 1992; Gébelin et al., 2011, 2015; Gottardi et al., 2011, 2015, 2018; Ingebritsen & Manning, 2010; Methner et al., 2015; Morrison, 1994; Morrison & Anderson, 1998; Mulch et al., 2004, 2007; Person et al., 2007; Quilichini et al., 2015, 2016; Wickham & Taylor, 1987), basinal brines (Roddy et al., 1988; Spencer & Welty, 1986), deep magmatic or metamorphic sources (Axen, 1992; Kerrich & Rehrig, 1987; Smith et al., 1991), or mixing of multiple sources (Quilichini et al., 2016; Spencer & Welty, 1986) (Figure 1). Yet, the stable isotope record of DSZs that have experienced protracted fluid flow is often difficult to interpret (e.g., Gébelin et al., 2013; Gottardi et al., 2015; Mulch et al., 2006), because despite being at "elevated temperatures" the ductile portion of detachment shear zones is still a retrograde system, where the thermal driving force for reaction and equilibration is lacking, and reaction progress is instead controlled by other factors such as the availability and composition of fluids (e.g., Gottardi et al., 2015). In particular, stable isotope data are strongly dependent on time-integrated water-rock ratios (e.g., Baumgartner & Valley, 2001; Ohmoto & Rye, 1974; Taylor, 1978). At mid-crustal levels, porosity and permeability are relatively small (e.g., Saar & Manga, 2004); thus, water-rock isotopic equilibrium is rock-dominated at low water-rock ratios. Therefore, assuming water-rock isotopic equilibrium, evolved meteoric fluids will have oxygen isotope compositions that are indistinguishable from metamorphic fluids, and the country rock will only show minor depletion in ^{18}O (e.g., Taylor, 1978). In addition, owing to exhumation, rock uplift, and associated changes in elevation and/or climate, the driving force and composition of the fluid entering the detachment shear zone evolve over time (e.g., Gébelin et al., 2012; Methner et al., 2015). At low water-rock ratios, this can lead to either multiple populations of metamorphic minerals with different isotopic compositions or progressive zoning/partial resetting of isotopic ratios within minerals. Finally, the detachment shear zone is a dynamic zone that transitions from ductile to brittle regimes at depths where fluid-rock exchange eventually ceases, and minerals must adjust to syn-kinematic changes in P–T–depth during exhumation of the detachment shear zone (e.g., Mulch et al., 2005) leading to complex overprinting and mixed signals in the isotopic proxies.

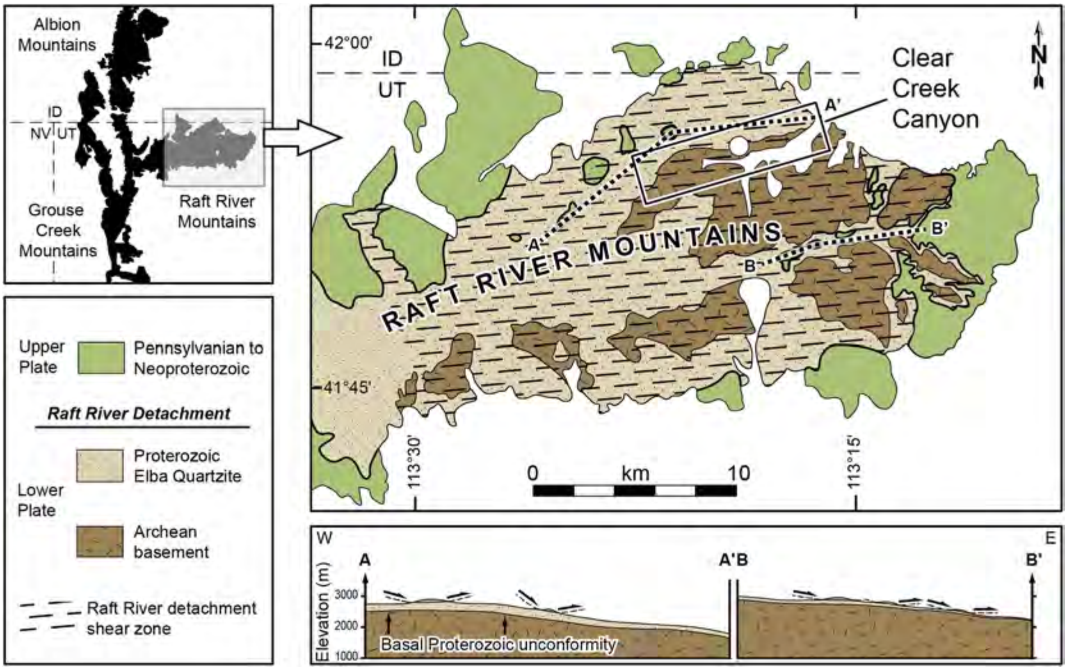

Figure 2. Geological map and cross-section of the Raft River Mountains and location of sampled sections (modified after Wells (2001), Sullivan (2008), Gottardi and Teyssier (2013)).

In this study, we explore how fluids penetrate the brittle-ductile transition, and how fluid-rock ratios affect the stable isotope record of DSZs. We focus our analysis on the Miocene Raft River DSZ (northwestern Utah), where the ubiquitous presence of meteoric fluids during deformation is well documented (Gottardi et al., 2011, 2015; Methner et al., 2015). We investigated the stable isotope composition of semi-brittle structures (high angle, transposed, and boudinaged quartz veins) as well as quartzite mylonite with varying muscovite content. Our results suggest that crack-seal events of semi-brittle structures (veins) provided fluid pathways for meteoric fluids to permeate the DSZ. ^{18}O and ^{2}H depletion of the quartzite mylonite correlates with muscovite content, suggesting that fluid facilitated the growth of muscovite and that fluid flow and higher fluid-rock ratios affected rocks with the most favorable hydrological properties (higher porosity and permeability). Our findings demonstrate that fluid flow in the Raft River DSZ was highly localized, which has an important consequence on our understanding of fluid-weakening processes and strain localization in the lithosphere.

2. The Raft River Detachment Shear Zone

The Raft River Mountains are a component of the larger Raft River-Albion-Grouse Creek metamorphic core complex, located in northwestern Utah's portion of the Great Basin province and in the hinterland of the Sevier Orogen (Figure 2; Compton, 1975). The Raft River Mountains were formed by orogenic collapse following several Mesozoic to early Cenozoic episodes of crustal shortening and thickening (e.g., Wells, 1997). The Raft River-Albion-Grouse Creek experienced two successive phases of extension and exhumation: a first episode from 73 to 42 Ma along the northwest-verging Middle Mountain Shear Zone (Figure 2; Saltzer & Hodges, 1988; Wells et al., 2000), and a second episode from ∼25 to 15 Ma along the east-verging Raft River DSZ (RRDSZ, Figure 2; Gottardi et al., 2015; Wells et al., 2000).

Only scattered klippen consisting of Paleozoic metasedimentary rocks remain of the hanging wall of the RRDSZ (Compton, 1975; Wells, 1997, 2001; Wells et al., 1998). The footwall is composed of the Green Creek Complex (Armstrong, 1968; Armstrong & Hills, 1967) consisting of ∼2.55 Ga gneissic monzogranite (Compton et al., 1977) overlain by the Proterozoic Elba Quartzite, which is where the RRDSZ is localized (Compton, 1975; Wells, 1997). The basement rocks below the Elba Quartzite show very little evidence of deformation, suggesting that the rheological contrast between the quartzite and basement caused strain localization within the Elba Quartzite (Gottardi & Teyssier, 2013; Malavieille, 1987; Sullivan, 2008; Wells, 2001).

The thickness of the Elba Quartzite varies across the Raft River Mountains as a result of Miocene shearing, ranging from ∼300 to 15 m from west to east (Wells et al., 2000). The Elba Quartzite displays a distinct stratigraphy that contains a basal quartzite cobble metaconglomerate, an alternating sequence of white quartzite and muscovite-quartzite schists, a distinctive layer of red quartzite and pure quartzite and a sequence of alternating feldspar-rich quartzite, pure quartzite, and pebble-gravel meta-conglomerate (Gottardi et al., 2015; Sullivan, 2008; Wells et al., 1998). Near the bottom half of the RRDSZ (∼10–20 m above the contact with the basement), the quartzite cliff makes a distinctive physiographic "notch." The notch is characterized by a zone of friable muscovite-rich quartzite associated with talc, kyanite, and massive quartz veins, contrasting with the quartzite (∼90% quartz, ∼10% muscovite) above and below (Gottardi et al., 2015).

The mylonitic fabric of the Elba Quartzite is consistent across the eastern Raft River Mountains. Mylonitic foliation is defined by elongated muscovite folia, and shallowly dips toward the East, conforming to the gentle domal shape of the metamorphic core complex (Compton, 1980; Gottardi & Teyssier, 2013; Sullivan, 2008; Wells, 1997). Stretched muscovite grains on the foliation planes define the lineation and clearly indicate a top-to-east sense of shear (Compton, 1980; Gottardi & Teyssier, 2013; Sullivan, 2008; Wells, 1997). Quartz microstructures and stable isotope geothermometry indicate that the Elba Quartzite deformed under greenschist-facies conditions during the Miocene (Gottardi & Teyssier, 2013; Gottardi et al., 2011, 2015).

Previous hydrogen and oxygen stable isotope analyses revealed the ubiquitous and protracted presence of fluids during evolution of the RRDSZ (Gottardi et al., 2011, 2015; Methner et al., 2015). The hydrogen stable isotope composition of synkinematic muscovite reveals that Eocene deformation along RRDSZ was characterized by low δ^2H_{fluid} of meteoric origin ($\delta^2H_{fluid} < -126$‰, Methner et al., 2015). Bulk hydrogen isotope analyses of fluid inclusions in quartz and synkinematic muscovite demonstrate that Miocene deformation along the RRDSZ was also associated with a low $^2H/^1H$ and $^{18}O/^{16}O$ of meteoric origin (-100‰ $< \delta^2H_{fluid} < -70$‰) (Gottardi et al., 2011, 2015).

3. Methods

3.1. Samples

The quartz vein population of the Elba Quartzite mylonite was investigated along three vertical transects across the RRDSZ (Figure 3), and representative oriented samples were collected for oxygen and hydrogen stable isotope analysis (Table 1). Additionally, quartzite mylonite samples with varying amounts of muscovite (from 5% to 20%) were collected across the "notch" area. Samples were prepared using conventional crushing and mineral separation techniques. Samples were cut into small slabs and edges were trimmed off, then pulverized, sieved, and washed. Mineral separates of quartz and muscovite were manually picked under a binocular microscope from the 500–250 μm grain size fraction to optically ensure mineral purity (e.g., no mineral inclusions). All stable isotope analyses were conducted at the Stable Isotope Lab at the University of Texas, Austin.

3.2. Hydrogen Stable Isotope Geochemistry

Hydrogen was extracted from ∼2 mg of muscovite separates using the methods outlined by Sharp et al. (2001). Mineral separates were powdered and loaded into silver capsules, and then pyrolized in a carbon reactor at 1450°C in a continuous flow of helium. Gasses derived are transferred to a ThermoElectron MAT 253 where δ^2H values are measured. Six standards were measured during the analyses: NBS-22 ($\delta^2H = -120$‰), IAEA-CH7 ($\delta^2H = -100$‰), USGS57 ($\delta^2H = -92$‰), USGS58 ($\delta^2H = -28$‰), internal talc standard ($\delta^2H = -40$‰), and internal serpentine standard ($\delta^2H = -126$‰). δ^2H values are reported relative to VSMOW. Error is ±2‰ (1σ), based on the reproducibility of standards from the analytical runs.

3.3. Oxygen Stable Isotope Geochemistry

Oxygen was extracted from ∼2 mg of quartz and muscovite separated by laser fluorination (Sharp, 1990). Samples were individually heated by a MIR10-30 laser in the presence of BrF_5. Using a series of liquid nitrogen traps, oxygen gas was cryogenically purified along a vacuum extraction system. Purified oxygen was collected on 5 Å sieve beads. Via heating, oxygen is injected into a dual bellows system where $\delta^{18}O$ values were measured by a ThermoElectron MAT 253 stable isotope ratio mass spectrometer. To ensure precision and accuracy, two standards, UWG-2 ($\delta^{18}O = +5.8$‰) (Valley et al., 1995), a garnet standard, and Lausanne-1 ($\delta^{18}O = +18.1$‰), an

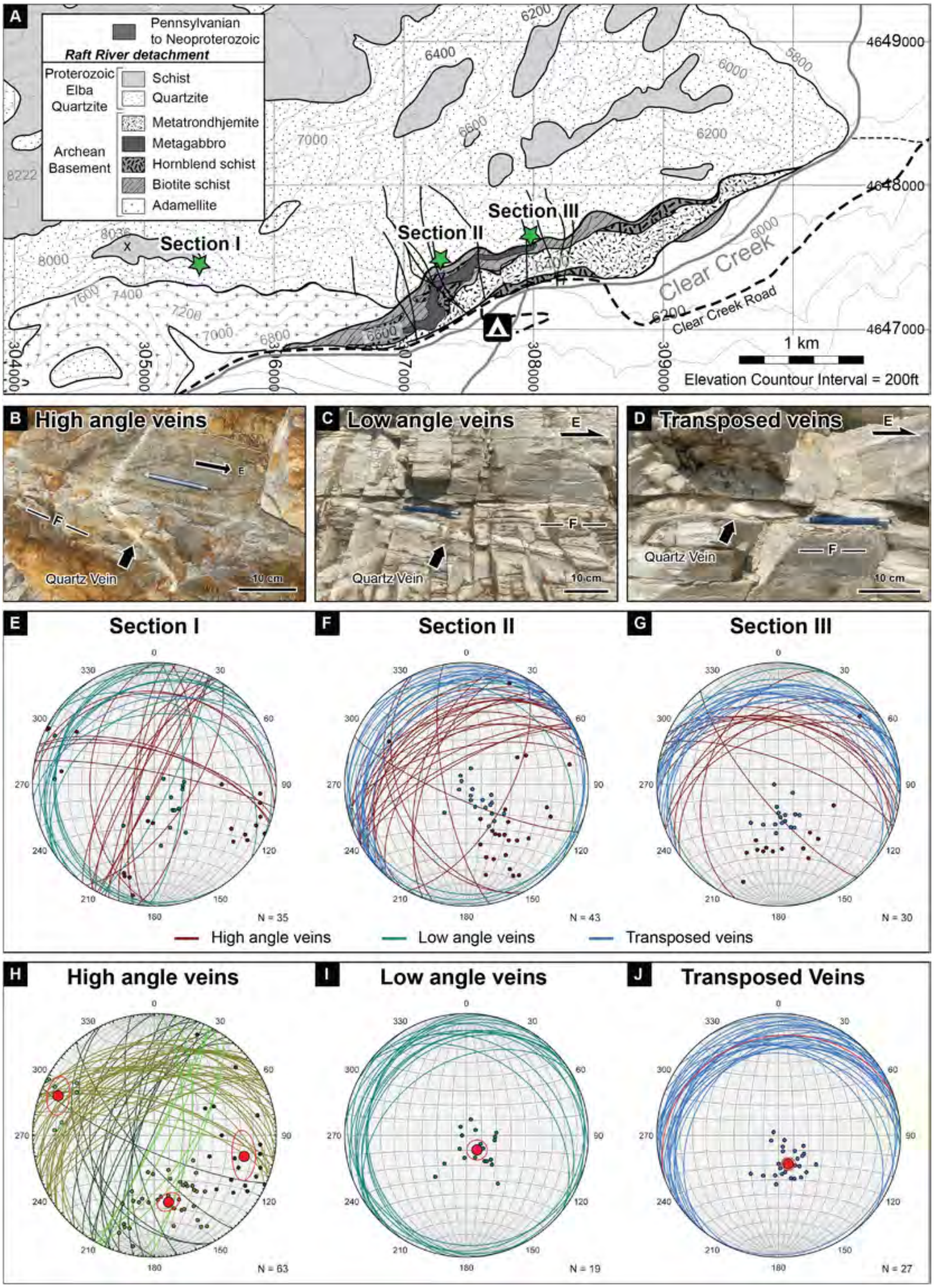

Figure 3. (a) Detailed geologic map of Clear Creek Canyon showing the location of the vertical transects (Section I, II, III) where vein orientation was measured and vein samples were collected (modified from Sullivan (2008) and Gottardi et al. (2015)). (b–f) Three types of veins were recognized in the field: high angle vein (b), low angle veins (c), and transposed veins (d). Orientation analysis of the field data reveals the presence of 3 clusters of high-angle veins (h). Low angle (i), and transposed veins (j) have consistent orientation throughout the study area.

Table 1

List of Representative Samples Selected for Oxygen and Hydrogen Stable Isotope Analysis

Sample #	Elevation (m above basement)	Description	Muscovite content	Locality	Latitude	Longitude
RR21-53	81	High angle vein	<5%	III	41.959085	−113.320861
RR21-60	74	High angle vein	<5%	I	41.921145	−112.619027
RR21-47	58	High angle vein	<5%	III	41.958820	−113.320270
RR21-45	50	Transposed vein	5%–10%	III	41.958634	−113.320172
RR21-40	40	High angle vein	<5%	III	41.958759	−113.320080
RR21-18	32	Transposed vein	5%–10%	II	41.957419	−113.326666
RR09-19	25	Quartzite schist	20%–25%	II	41.957563	−113.327137
RR09-18	24	Quartzite schist	20%–25%	II	41.957563	−113.327137
RR21-11	24	Transposed vein	5%–10%	II	41.957398	−113.327161
RR09-15	24	Quartzite	10%–15%	II	41.957563	−113.327137
RR09-14	23	Quartzite	10%–15%	II	41.957563	−113.327137
RR21-37	21	Transposed vein	5%–10%	II	42.023519	−112.845116
RR09-13	21	Quartzite	10%–15%	II	41.957563	−113.327137
RR09-12	19	Quartzite	10%–15%	II	41.957563	−113.327137
RR21-69	19	Transposed vein	5%–10%	I	41.955942	−113.349003
RR09-11	18	Quartzite	8%–12%	II	41.957563	−113.327137
RR09-10	17	Quartzite	8%–12%	II	41.957563	−113.327137
RR21-01	6	Transposed vein	5%–10%	II	41.957683	−113.325439

Note. See Figure 3 for localities on detailed geologic map. Latitude and longitude reported in UTM coordinate.

internal quartz standard, were measured along with mineral separates. $\delta^{18}O$ values are reported relative to SMOW, where the $\delta^{18}O$ value of NBS-28 is +9.6‰. Error is ±0.08‰ (1σ), based on the reproducibility of standards from the analytical run.

3.4. Fluid-Rock Ratios

Water-to-rock ratio (W/R) is a primary mechanism determining the amount of isotopic alteration that occurs within a mineral interacting with water (Ohmoto & Rye, 1974). Water-to-rock ratio is the weight ratio between rock and water within the system (Taylor, 1978). As soon as water enters the system, hydrogen isotopes begin equalizing between the rock and the water, leading to a large change in rock δ^2H toward the water-rock fractionation (Taylor, 1978). It is not until there is a significant influx of water (typically a $W/R > 0.1$) that the rock $\delta^{18}O$ value becomes greatly affected. A rock-dominated system will have a W/R of less than 1.0, whereas a water-dominated system will have a W/R greater than 1.0. By estimating the initial conditions of the system prior to water influx, the W/R ratio can be estimated by comparing the plot of Equations 1 and 2 below (from Ohmoto and Rye (1974)) against sample data.

$$\delta^{18}O_r^f = \frac{\delta^{18}O_r^i - \Delta^{18}O_{r-w} + \frac{89.79\%}{\%\ \mathrm{O\ in\ mineral}} * \frac{\mathrm{W}}{\mathrm{R}} * \delta^{18}O_r^i}{1 + \frac{89.79\%}{\%\ \mathrm{O\ in\ mineral}} * \frac{\mathrm{W}}{\mathrm{R}}} + \Delta^{18}O_{r-w} \tag{1}$$

$$\delta^{2}H_r^f = \frac{\delta^{2}H_r^i - \Delta^{2}H_{r-w} + \frac{11.19\%}{\%\ \mathrm{H\ in\ mineral}} * \frac{\mathrm{W}}{\mathrm{R}} * \delta^{2}H_r^i}{1 + \frac{11.19\%}{\%\ \mathrm{H\ in\ mineral}} * \frac{\mathrm{W}}{\mathrm{R}}} + \Delta^{2}H_{r-w} \tag{2}$$

where $\delta^{18}O_r^i$ and $\delta^2H_r^i$, and $\delta^{18}O_r^f$ and $\delta^2H_r^f$ are the initial and final $\delta^{18}O$ and δ^2H composition of the rock, respectively, and $\Delta^{18}O_{r-w}$ and Δ^2H_{r-w} are the oxygen and hydrogen isotopic fractionation coefficients between rock and water. Note that percentage H and O in the mineral is the weight percentage, and W/R represents the water to rock ratio in weight.

Table 2

Summary Table of the Average Strike and Dip of the Different Types of Veins Measured in the Field

Vein type		Strike	Dip
High Angle	Cluster 1	22 ± 6°	74 ± 10°
	Cluster 2	194 ± 12°	65 ± 10°
	Cluster 3	258 ± 9°	47 ± 6°
Low Angle		252 ± 9°	20 ± 9°
Transposed		234 ± 7°	12 ± 7°

Note. Averages are calculated based on maximum spherical eigenvalues with a 95% confidence using Orient (Vollmer, 2015, 2023).

4. Results

4.1. Structural Analysis

Field observations revealed the presence of three different types of quartz veins that we refer to as (a) high angle veins, (b) low angle veins, and (c) transposed veins (Table 2, Figure 3). High angle veins are the most abundant and cut the mylonitic foliation at high angle (~70 ± 10°) (Figure 3b). They tend to be narrow (1–5 cm wide) and extend up to ~1 m. Cluster analysis performed in Orient (Vollmer, 2015, 2023) revealed the presence of three sets of high angle veins (Table 2) striking at 22°, 194°, and 258° (Figure 3e). Low angle veins have shallow dips and appear stretched parallel to the extension direction (Figure 3c). These veins range in thickness from ~0.5 to 5 cm and extend up to ~1 m. Low angle veins approximately strike east west (252 ± 9°), and dip toward the north (20 ± 9°). The last type of veins is transposed subparallel to the foliation and forms well-developed boudins reaching up to ~10 cm in thickness (Figure 3d). Some of these transposed veins are stretched up to 1 m in the lineation direction. Transposed veins also strike approximately east-west (~234 ± 7°), and dip gently toward the north (~12 ± 7°).

4.2. Microstructural Analysis

4.2.1. High Angle Quartz Veins

The high angle quartz veins consist of large ribbon grains with moderate aspect ratios (1:3–1:8) that make up ~80%–90% of the vein area of the thin sections (Figures 4a and 4b). The geometry of the ribbons ranges from lozenge- to fish-shape with a slight asymmetry that is compatible with the top-to-the-east sense of shear within the DSZ. Ribbons commonly display sweeping undulose extinction and contain abundant deformation lamellae (Figures 4a and 4d). Evidence of minor dynamic recrystallization by dislocation creep, dominantly by subgrain rotation, is recorded within large ribbons and also along ribbon boundaries as bands of recrystallized grains (Figure 4b). Fluid inclusion planes are abundant within the ribbons (Figure 4b). Muscovite grains are scarce and hardly visible, occurring as microscopic flakes (~10–50 μm long, 1–10 μm thick) between quartz ribbons (Figure 4g).

4.2.2. Low Angle Quartz Veins

The low angle quartz veins also contain large ribbon grains that are oriented sub-parallel to the mylonitic foliation (Figure 4c), giving a foliated texture to these samples. Ribbons also show undulose extinction and contain deformation lamellae. Dynamic recrystallization by subgrain rotation is the dominant quartz deformation mechanism. Recrystallized grains are more abundant than in high angle quartz veins, representing up to 40% of the vein area of the thin sections. Some of the large ribbons show extensive recrystallization, forming relict grains surrounded by dynamically recrystallized subgrains (Figure 4d). Muscovite grains are found in rare layers oriented sub-parallel to the foliation (Figure 4c), and commonly pin larger quartz grains. Muscovite grains are generally long (~100–250 μm) and thin (10–25 μm) and show little internal deformation (Figure 4h).

4.2.3. Transposed Quartz Veins

In the transposed veins, most of the grains have recrystallized by subgrain rotation (Figures 4e and 4f); ribbons only occupy ~10% of the vein area of the thin sections. Relict grains are abundant and are typically characterized by undulose extinction and deformation of lamellae (Figure 4f). These samples have a well-developed foliation parallel to the mylonitic foliation in the host quartzite. Recrystallized grains form a secondary oblique foliation oriented 20°–30° to the mylonitic foliation defining Type II S-C fabrics (Lister & Snoke, 1984) consistent with a top-to-the-east sense of shear. Muscovite grains are large (>250 μm long, up to 100 μm thick) and abundant in the transposed veins, where they typically form fish with tails oriented parallel to the mylonitic foliation. Internal deformation of the muscovite fish occurs primarily by basal slip.

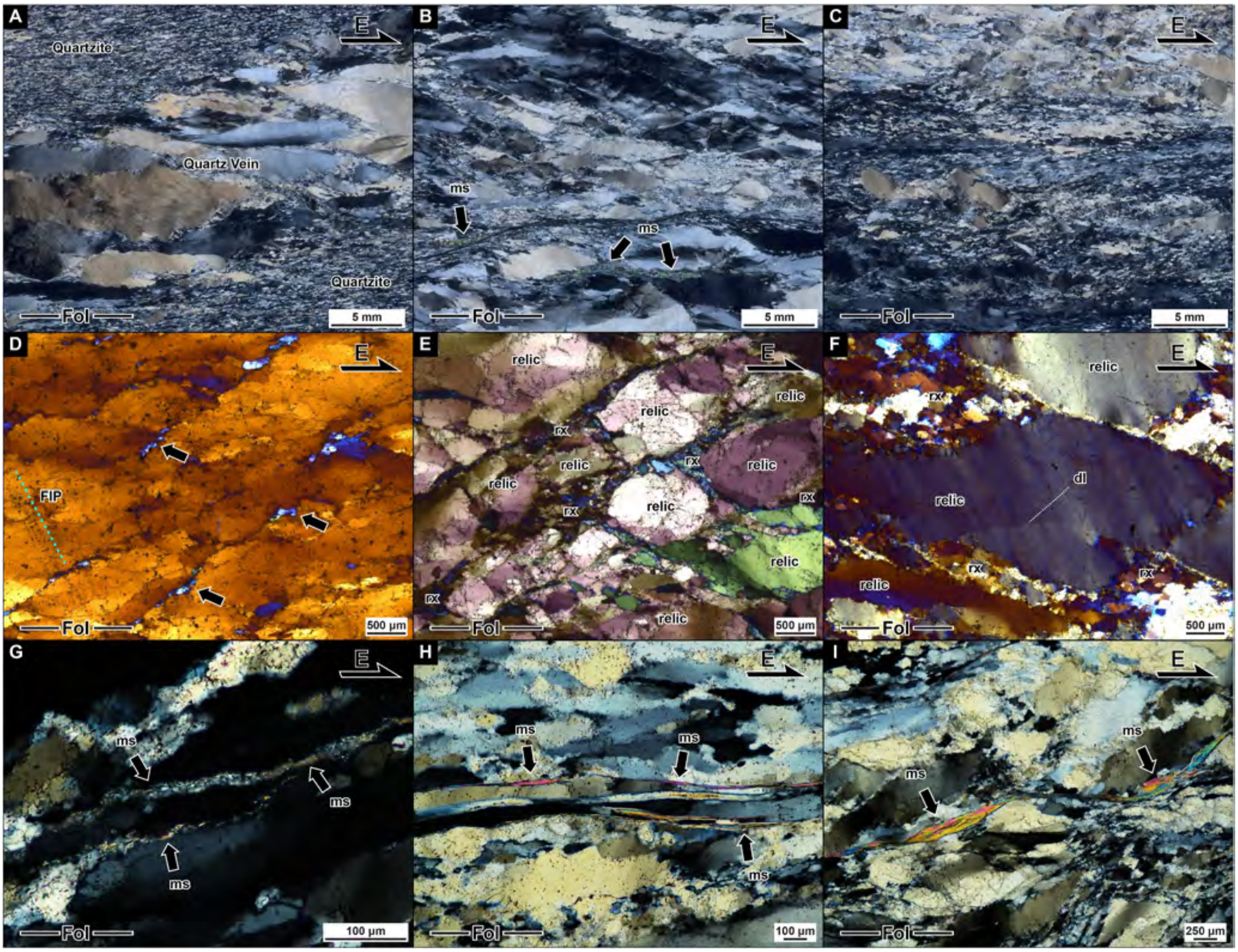

Figure 4. Representative microstructures of the three types of veins found within the study area: (a) high angle veins, (b) low angle veins, and (c) transposed veins. (d) In the high angle veins, quartz ribbons show incipient dislocation creep recrystallization by subgrain rotation (black arrows). Fluid inclusion planes (FIPs) are common. In the low-angle (e) and transposed (f) veins, respectively, progressive recrystallization by subgrain rotation produces a relic and recrystallized grain texture. Ribbons and large relic grains are typically characterized by sweeping undulose extinction and deformation of lamellae (dl). (g) In the high angle veins, muscovite grains (ms) occur as microscopic flakes (∼10–50 μm long, 1–10 μm thick) typically between quartz ribbons. (h) In the low angle veins, muscovite grains are larger (∼100–250 μm long, 10–25 μm thick), and begin to form layers conforming to the mylonitic foliation. (i) Muscovite grains are the largest (>250 μm long, up to 100 μm thick) and most abundant in the transposed veins, where they typically form fish with tails oriented parallel to the mylonitic foliation. Thin sections were oriented perpendicular to the mylonitic foliation and parallel to the mylonitic lineation. Photomicrographs taken in cross-polarized light (a–i), and with the gypsum plate (d–f).

4.3. Hydrogen Stable Isotopes

Only 5 of the vein samples contained muscovite, and muscovite hydrogen stable isotope data (δ^2H_{ms}) ranges from −125 to −88‰ (Table 3, Figure 5). The highest δ^2H_{ms} value (−88‰, RR21-45) is found toward the top of the section, whereas the lowest value is found near the bottom (−125‰, RR21-01). The quartzite mylonite shows less negative hydrogen stable isotope data ranging from −87 to 77‰ (Table 3, Figure 5). Our results fall within the range of δ^2H_{ms} (−125 to −72‰) previously reported by Gottardi et al. (2011, 2015).

The hydrogen stable isotope composition of fluid inclusions in quartz (δ^2H_{FI}) has previously been measured by Gottardi et al. (2015), and ranges from −104 to −83‰ with no systematic variation with structural position (Figure 5). Using the calibration of Suzuoki and Epstein (1976) and an exchange temperature of 400 ± 50°C, the calculated fractionation between fluid and muscovite ($\Delta^2H_{H2O\text{-}ms}$) ranged from 23 to 38‰. At such temperatures, fluid with a composition of $-104‰ < \delta^2H_{H2O} < -83‰$ in equilibrium with muscovite would have produced δ^2H_{ms} values as low as −127‰. The measured δ^2H_{ms} values fall within that range; therefore, muscovite either neocrystallized from the fluid or recrystallized in the presence of the fluid that was present during deformation, which is preserved in the fluid inclusions.

Table 3

Oxygen Isotope Results of Quartz ($\delta^{18}O_{qtz}$) and Muscovite ($\delta^{18}O_{ms}$), Quartz-Muscovite Oxygen Isotope Fractionation ($\Delta^{18}O_{qtz\text{-}ms}$), Temperature of Equilibrium Calculated Based on Chacko et al. (1996) Quartz-Muscovite Calibration, and Hydrogen Isotope Results of Muscovite (δ^2H_{ms})

Sample	$\delta^{18}O_{qtz}$ (‰)	$\delta^{18}O_{ms}$ (‰)	$\Delta^{18}O$ (‰)	T (°C)	δ^2H_{ms} (‰)
Transposed Quartz Veins					
RR21-01	10.1	7.5	2.6	460	−125
RR21-11	11.5	8.3	3.2	390	−106
RR21-18	11.5	7.8	3.7	350	−112
RR21-37	12.1	9.5	2.6	460	−108
RR21-45	12.1	8.7	3.4	370	−88
RR21-69	9.1				
High Angle Quartz Veins					
RR21-40	10.1				
RR21-47	10.6				
RR21-53	11.0				
RR21-60	10.7				
Quartzite mylonite data from the notch					
RR09-10	10.8	10.1	0.7		−100
RR09-11	11.0	10.1	0.9		−101
RR09-12[a]	11.5	8.0	3.5	360	−83
RR09-13	11.6	11.2	0.4		−77
RR09-14	11.4	10.4	1.0		−86
RR09-15	11.8	10.4	1.4		−77
RR09-18[a]	12.4	8.3	4.1	310	−101
RR09-19[a]	11.2	7.8	3.4	370	−110

Note. $\delta^{18}O$ and δ^2H values are reported relative to SMOW; error is ±0.08‰ (1σ) and ±2‰ (1σ) for oxygen and hydrogen, respectively, based on the reproducibility of standards from the analytical runs. [a]Indicates samples with >20% muscovite.

4.4. Oxygen Stable Isotopes

The $\delta^{18}O$ value was measured in quartz in all samples and muscovite where present (Table 3 and Figure 6). The quartz $\delta^{18}O$ ($\delta^{18}O_{qtz}$) and muscovite $\delta^{18}O$ ($\delta^{18}O_{ms}$) values range between 9.1 and 12.1‰ and 7.5 and 9.5‰, respectively. The highest and lowest quartz $\delta^{18}O$ values are found in transposed veins ($\delta^{18}O_{qtz} = 9.1‰$ for RR21-37 and $\delta^{18}O_{qtz} = 12.1‰$ for RR21-45). The high angle veins seem to show a slight trend toward lower $\delta^{18}O$ with depth, with $\delta^{18}O_{qtz} = 11.0‰$ (RR21-53) at the top of the section, decreasing to $\delta^{18}O_{qtz} = 10.1‰$ (RR21-40) right above the notch. The lowest $\delta^{18}O_{qtz}$ (9.1‰) is measured in the notch (RR09-69). The $\delta^{18}O$ values of muscovite also display a general trend toward lower values with depth, ranging from 8.7‰ near the top of the section (RR09-45) to 7.5‰ near the bottom (RR21-01). The highest $\delta^{18}O_{ms}$ value (9.5‰) is measured in the notch (RR21-69).

The quartz-muscovite oxygen isotope fractionation ($\Delta^{18}O_{qtz\text{-}ms}$) is temperature dependent and can be used to estimate the temperature of oxygen isotopic exchange, using the Chacko et al. (1996) quartz-muscovite geothermometer. The $\Delta^{18}O_{qtz\text{-}ms}$ ranges from 2.6 to 3.7‰, suggesting an equilibrium temperature ranging from 350 to 460°C (Table 3; Figure 7). Note that the only samples containing enough muscovite and enabling temperature of equilibrium calculation are transposed veins; none of the high-angle veins contained enough muscovite to be measured.

4.5. Fluid-Rock Ratio Models

Water-to-rock ratio (W/R) is a primary control determining the amount of isotopic alteration that occurs within a mineral (Ohmoto & Rye, 1974; Taylor, 1978). The combined results of oxygen and hydrogen stable isotope analysis can be plotted on a fluid-rock depletion model, showing δ^2H_{ms} versus $\delta^{18}O_{qtz}$ for different fluid-rock ratios (Figure 8). Our results are plotted along the Global Meteoric Water Line ($\delta^2H = 8.0 \times \delta^{18}O + 10‰$). Using Equations 1 and 2, we generate eight water-depletion curves based on specific original rock and fluid isotopic composition inputs to model the final composition of muscovite and quartz at different fluid-rock ratios (Figure 8). Modeling parameters for the depletion models are summarized in Table 4. We use a temperature of equilibrium of 400°C, which has been previously determined as the mean temperature for the most equilibrated samples of this study, as well as the average temperature defined in Gottardi et al. (2011, 2015).

The initial $\delta^{18}O_{qtz}$ and δ^2H_{ms} values for the quartz and muscovite, respectively, were taken as the highest values measured in the section, inferred as "protolithic" or representing the composition of the minerals before isotopic exchange. We used $\delta^2H_{rock,\ initial\ 1} = -65‰$ or $\delta^2H_{rock,\ initial\ 2} = -80‰$, and $\delta^{18}O_{rock,\ initial\ 1} = 12‰$ or $\delta^{18}O_{rock,\ initial\ 2} = 14‰$, as these values are the highest measured in Gottardi et al. (2015), and thus came into contact with the least amount of fluid causing the least alteration from the initial isotopic state. This gives us four possible starting compositions (black squares labeled a–d in Figure 8).

We then use two initial water compositions, one based on meteoric water composition, and one based on an evolved fluid. In both cases, the initial water hydrogen isotope composition was chosen based on the composition of fluid inclusions ($\delta^2H_{water,\ initial\ 1} = -100‰$), which likely represents pristine meteoric water (Gottardi et al., 2015). In the first case, the initial water oxygen isotope composition was calculated based on $\delta^2H_{water,\ initial\ 1} = -100‰$ using the global meteoric water line (GMWL) equation ($\delta^{18}O_{water,\ initial\ 1} = -13.75‰$) (solid and dashed dark blue lines on Figure 8). Because of the differences in the extent of δ^2H and $\delta^{18}O$ isotope exchange observed in our results, it is possible that the δ^2H and $\delta^{18}O$ composition of the initial fluid becomes decoupled along an extended flow path, with δ^2H remaining near its initial meteoric value and $\delta^{18}O$ progressively shifting toward a rock-like

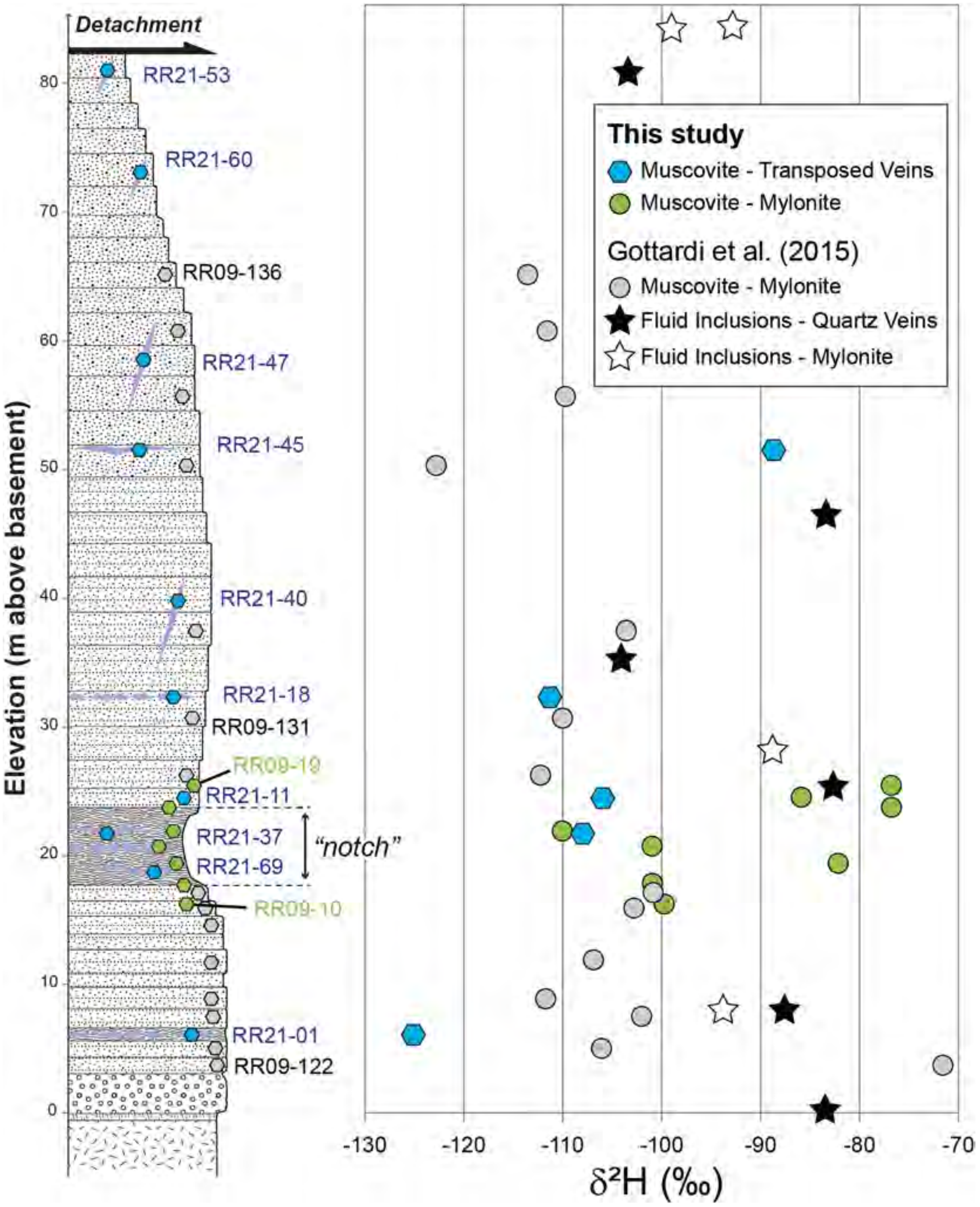

Figure 5. Compilation of δ^2H values from this study and Gottardi et al. (2015).

value with depth. Therefore, using the global meteoric water line to calculate initial $\delta^{18}O$ of the interacting fluid may not be adequate. For this reason, we also use a starting fluid composition of $\delta^2H_{\text{water, initial 2}} = -100‰$ but with a $\delta^{18}O$ shifted toward a rock-like value ($\delta^{18}O_{\text{water, initial 2}} = 0‰$) (dashed and solid cyan lines on Figure 8).

Finally, the $\Delta^2H_{\text{rock-water}}$ was calculated using the calibration of Suzuoki and Epstein (1976) ($\Delta^2H_{\text{rock-water}} = -29.7‰$), and the $\Delta^{18}O_{\text{rock-water}}$ was calculated using the calibration of Sharp and Kirschner (1994) ($\Delta^{18}O_{\text{rock-water}} = 5.2‰$). Rock weight percentages are simply the weight percentages of oxygen and hydrogen within the stoichiometry of their respective minerals.

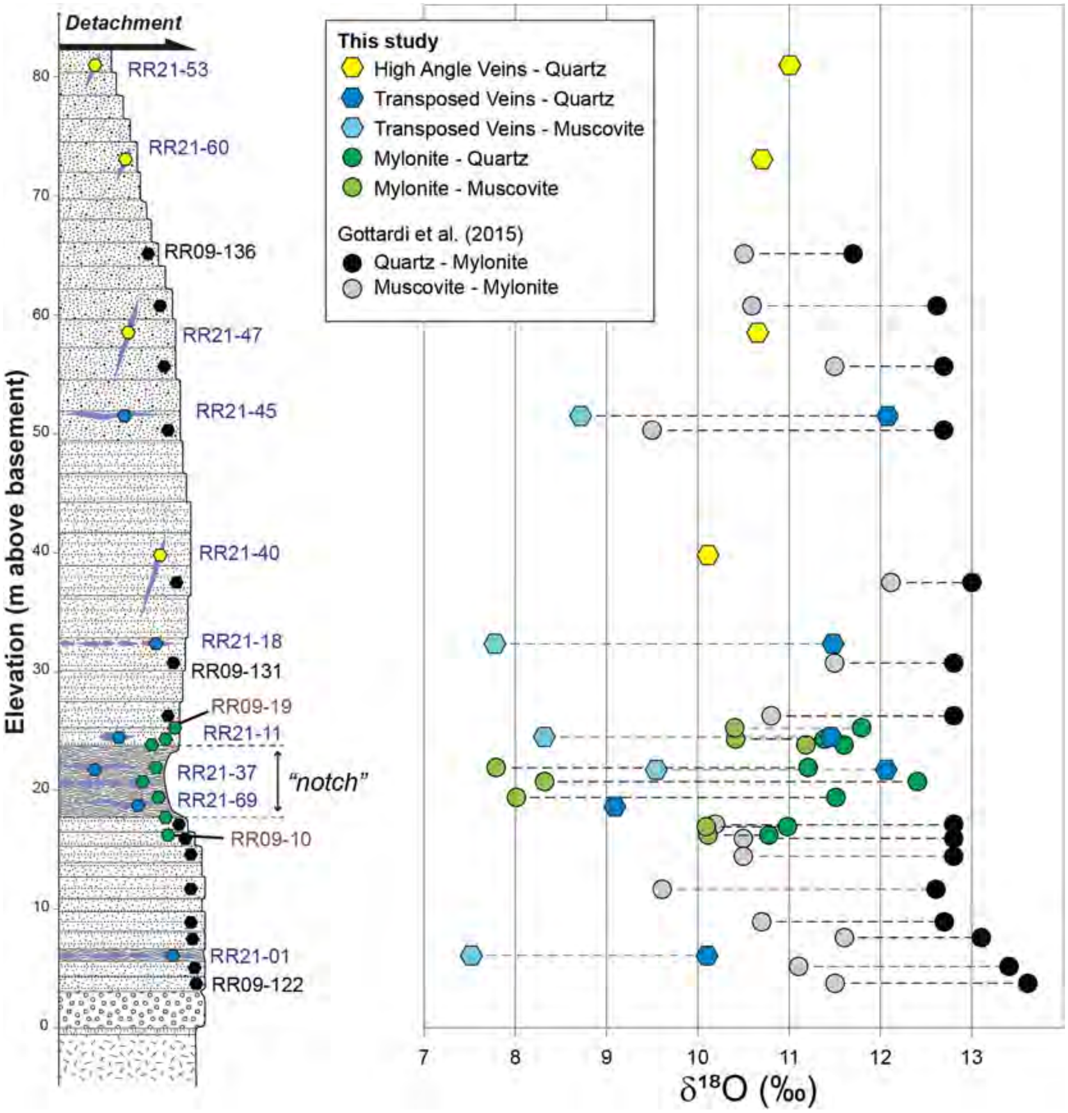

Figure 6. Compilation of $\delta^{18}O$ values from this study and Gottardi et al. (2015).

Our results, along with data from Gottardi et al. (2015) fall between our eight models at W/R smaller than 0.1 (Figure 8). The quartzite samples from the notch area fall very close to our model using input parameters of $\delta^2H_{\text{rock, initial 1}} = -65‰$ and $\delta^{18}O_{\text{rock, initial 1}} = 12‰$. Some of these samples indicated that they barely exchanged with a fluid ($W/R < 0.005$). The quartzite mylonite from Gottardi et al. (2015) falls closer to the model using the other input parameters ($\delta^2H_{\text{rock, initial 2}} = -80‰$ and $\delta^{18}O_{\text{rock, initial 2}} = 14‰$, Figure 8), values that suggest a "protolith" $\delta^{18}O$ composition that was higher than in the notch area. These quartzite mylonites show interaction with a fluid at low W/R ($0.01 < W/R < 0.05$). Quartz veins fall between our two models in a similar range of W/R ratios (Figure 8). Initial $\delta^{18}O$ water composition affects the "knee" of the curve—more evolved fluid composition shifts the knee toward higher $\delta^{18}O$. The quartzite mylonites from Gottardi et al. (2015) may fit better between the curves using the more evolved initial fluid composition. However, initial $\delta^{18}O$ fluid composition does not appear to make much of a difference in the W/R ratios. All of our results suggest that fluid-rock exchange occurred in a rock-dominated system.

5. Discussion

In this discussion, we interpret our data in the context of other extensive stable isotope data sets from Gottardi et al. (2015) collected in the same study area. Gottardi et al. (2015) analyzed 15 samples of quartzite mylonites

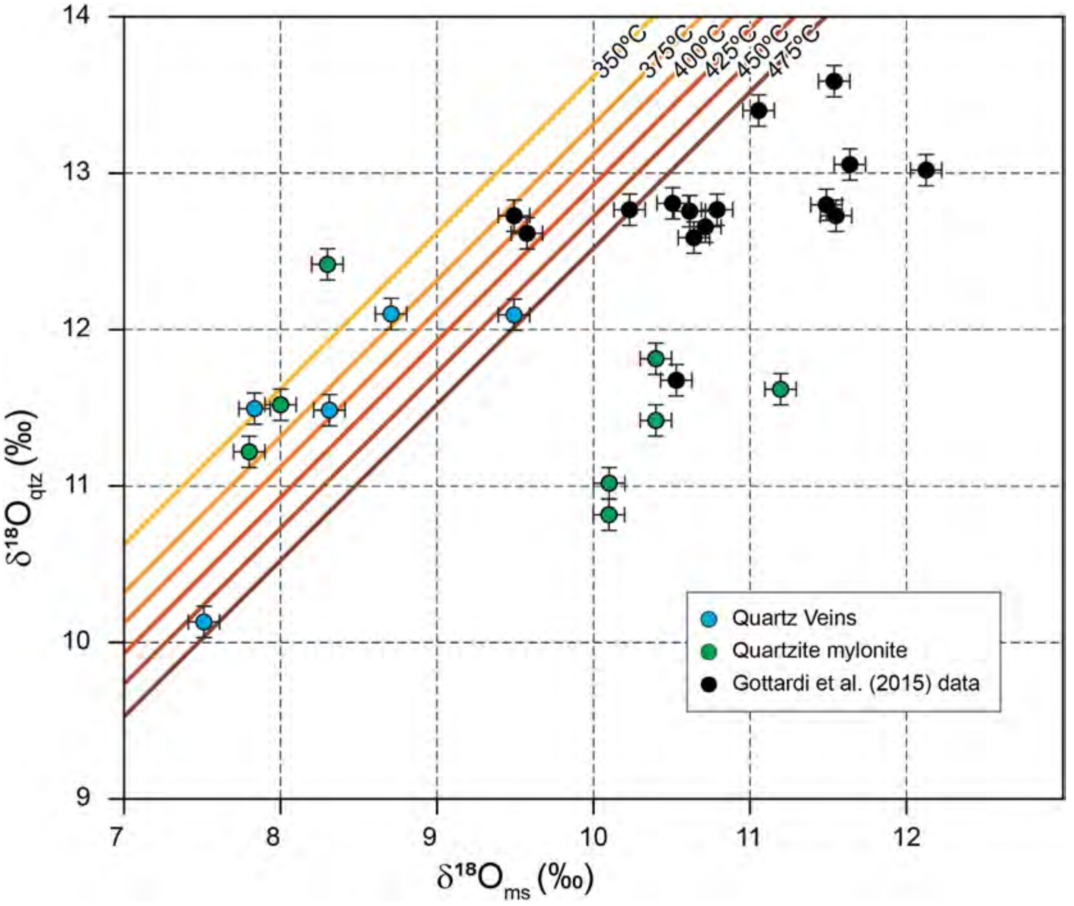

Figure 7. $\delta^{18}O$ of quartz ($\delta^{18}O_{qtz}$) versus $\delta^{18}O$ of muscovite ($\delta^{18}O_{ms}$) values from quartz veins and mylonitic quartzite analyzed in this study, as well as mylonitic quartzite data sets from Gottardi et al. (2015). Temperatures correspond to lines of constant oxygen isotope fractionation using the Chacko et al. (1996) quartz-muscovite geothermometer.

containing less than 10% muscovite, referred to in the following as muscovite-poor quartzite mylonites. Our 8 quartzite mylonite samples collected in the notch area contained varying amounts of muscovite (~5%–25%), which we refer to as muscovite-rich quartzite mylonites; 3 of these samples contained >20% muscovite (see Table 2).

5.1. Fluid Source

Our results are in agreement with previous stable isotope investigations of the Raft River metamorphic core complex that demonstrated that meteoric fluids characterized by low ^2H/low ^{18}O penetrated the brittle-ductile transition during Miocene shearing and exhumation of the RRDSZ (Gottardi et al., 2011, 2015; Methner et al., 2015). The hydrogen stable isotope composition of muscovite measured in this study ($-125‰ < \delta^2H_{ms} < -77‰$, Table 3) falls within the range of other data sets for the same area ($-125‰ < \delta^2H_{ms} < -72‰$; Figure 5; Gottardi et al., 2011, 2015; Methner et al., 2015). At the temperature of deformation previously estimated for the RRDSZ (400 ± 50°C; Gottardi et al., 2011, 2015), the fractionation between muscovite and the water present would range from 23 to 38‰, yielding a hydrogen stable isotope composition for the water as low as −101‰ (using the calibration of Suzuoki and Epstein (1976)). This δ^2H_{fluid} is compatible with the composition of fluid inclusions in quartz ($-104‰ < \delta^2H_{FI} < -83‰$) previously measured by Gottardi et al. (2015) along the same vertical profile. Such δ^2H_{fluid} composition suggests that the fluid present during deformation was meteoric in origin, with a composition of $\delta^2H_{fluid} \approx -100‰$ corresponding to a $\delta^{18}O_{fluid} \approx -13.75‰$ (using the meteoric water line).

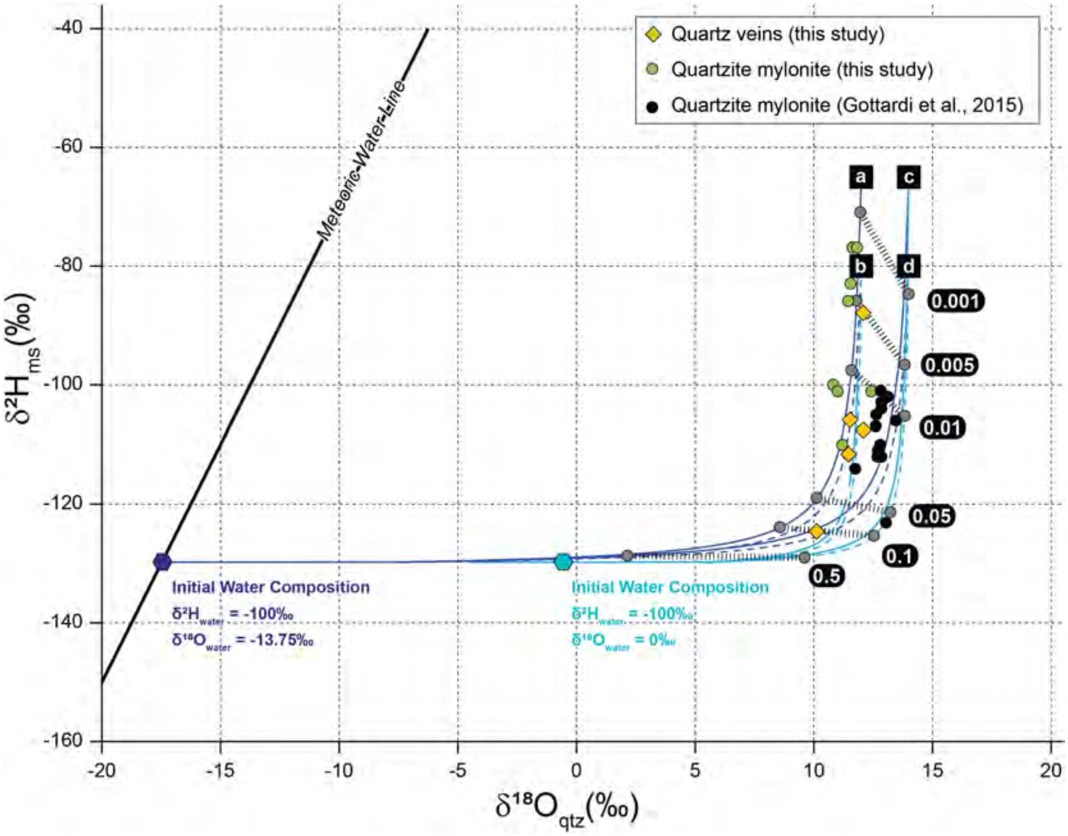

Figure 8. Calculated muscovite δ^2H_{ms} and quartz $\delta^{18}O_{qtz}$ composition modeled for different water-rock ratios using a temperature of 400°C. Measured δ^2H_{ms} and $\delta^{18}O_{qtz}$ data is plotted for quartz veins and mylonites from this study and Gottardi et al. (2015). The initial endmember isotope values are based on assuming "unaltered" muscovite isotopic composition of $\delta^2H_{\text{rock initial}}$ of −65‰ and −80‰ and $\delta^{18}O_{\text{rock, initial}}$ of 12 and 14‰, leading to four initial rock compositions (a) $\delta^2H_{\text{rock initial}} = -65$‰ and $\delta^{18}O_{\text{rock, initial}} = 12$‰, (b) $\delta^2H_{\text{rock initial}} = -80$‰ and $\delta^{18}O_{\text{rock, initial}} = 12$‰, (c) $\delta^2H_{\text{rock initial}} = -65$‰ and $\delta^{18}O_{\text{rock, initial}} = 14$‰, (d) $\delta^2H_{\text{rock initial}} = -80$‰ and $\delta^{18}O_{\text{rock, initial}} = 14$‰. We used two initial water compositions to calculate our depletion curves, one strictly meteoric ($\delta^2H_{\text{water, initial 1}} = -100$‰, $\delta^{18}O_{\text{water, initial 1}} = -13.75$‰, solid and dashed dark blue line), and one evolved ($\delta^2H_{\text{water, initial 2}} = -100$‰, $\delta^{18}O_{\text{water, initial 2}} = 0$‰, solid and dashed cyan lines). See text for details and Table 4 for a summary of input parameters.

5.2. Fluid-Rock Exchange in the Quartzite Mylonite

The oxygen isotope composition of quartz and muscovite reveals the following trends. The muscovite-poor quartzite mylonites consistently exhibit the highest $\delta^{18}O_{qtz}$ values across the RRDSZ (11.7‰ < $\delta^{18}O_{qtz}$ < 13.5‰, Table 3, Figure 6). This observation suggests that quartz in the muscovite-poor quartzite mylonites only experienced limited interaction with meteoric fluid. A similar trend is observed in the muscovite although $\delta^{18}O_{ms}$ displays a larger range of values (9.4‰ < $\delta^{18}O_{ms}$ < 12.1‰). Consequently, in these rocks, quartz-muscovite oxygen isotope fractionation ($\Delta^{18}O_{qtz\text{-}ms}$) exhibits a wide range of values (0.9‰ < $\Delta^{18}O_{qtz\text{-}ms}$ < 3.3‰). The temperature of deformation for the RRDSZ has previously been estimated at 400 ± 50°C (Gottardi et al., 2011, 2015), which correlates to a $\Delta^{18}O_{qtz\text{-}ms}$ ranging from 2.7 to 3.6‰ using the calibration of Chacko et al. (1996). If all muscovite-poor samples had reached isotopic equilibrium, we would expect the $\Delta^{18}O_{qtz\text{-}ms}$ to show similar values. However, only 3 out of the 15 samples of muscovite-poor mylonite fall within that range (Table 3). This disparity in $\Delta^{18}O_{qtz\text{-}ms}$ can be explained either by (a) different extents of fluid-rock interaction at various W/R ratios or (b) isotope exchange over different times, varying temperatures, and/or with variable fluid compositions—that is, true disequilibrium.

If our isotopic fractionations represent different extents of equilibrium reactions with the same meteoric fluid at various W/R ratios, then we assume the presence of spatial isotopic heterogeneity within the footwall of the RRDSZ—certainly at the scale of sampling within outcrops and quite possibly at scales smaller than the sampling

Table 4

Input Parameters Used in the Plot of Calculated δ^2H_{ms} and $\delta^{18}O_{qtz}$ at Different Fluid-Rock Ratios Shown in Figure 8

Parameter	Value	Source
Temperature	400°C	Gottardi et al. (2015)
Hydrogen		
$\delta^2H_{\text{rock, initial 1}}$	−65‰	Gottardi et al. (2015)
$\delta^2H_{\text{rock, initial 2}}$	−80‰	Gottardi et al. (2015)
$\delta^2H_{\text{water, initial 1}}$	−100‰	Gottardi et al. (2015)
$\delta^2H_{\text{water, initial 2}}$	−100‰	Gottardi et al. (2015)
$\Delta^2H_{\text{rock-water}}$	−29.7‰	Suzuoki and Epstein (1976)
rock weight % H	0.51%	Calculated
Oxygen		
$\delta^{18}O_{\text{rock, initial 1}}$	12‰	Gottardi et al. (2015)
$\delta^{18}O_{\text{rock, initial 2}}$	14‰	Gottardi et al. (2015)
$\delta^{18}O_{\text{water, initial 1}}$	−13.75‰	Calculated from GMWL
$\delta^{18}O_{\text{water, initial 2}}$	0‰	
$\Delta^{18}O_{\text{rock-water}}$	5.2‰	Sharp and Kirschner (1994)
rock weight % O	53.26%	Calculated

volume of grain separates on which isotope measurements were made. In this case, the variability of our results is a consequence of the scale of the isotope measurement being larger than the scale of isotope exchange. That is, our isotope measurements are sampling and probably mixing the spatial isotopic heterogeneity, resulting from different proportions of mixing between exchanged (veins and muscovite rich quartzites), partially exchanged (quartzite and muscovite rich quartzite) and unexchanged (some samples of quartzite mylonite) mineral volumes during measurement. Indeed, at low fluid-rock ratios, the system remains rock-dominated, and limited fluid availability prevents quartz and muscovite from exhibiting significant ^{18}O depletion, hence the preservation of the original isotopic composition. At high fluid-rock ratios, quartz and muscovite interact with a volume of fluid large enough to be reflected in their lower $\delta^{18}O$ values. Differences in fluid-rock ratio are further explored in Section 5.4. Alternatively, quartz and muscovite may not have reached isotopic equilibrium at the scale at which their isotope composition is being measured. In this case, quartz and muscovite exchanged differentially, either over different time scales, different temperature ranges, or even with different generations of fluid.

Interestingly, muscovite-rich quartzites (>20% muscovite) of the notch show fractionation consistent with the deformation temperature ($3.4‰ < \Delta^{18}O_{\text{qtz-ms}} < 4.1‰$, Table 3; Figure 6), suggesting that they reached isotopic equilibrium, whereas the fractionation in the muscovite-poor quartzite is much smaller ($0.7‰ < \Delta^{18}O_{\text{qtz-ms}} < 1.4‰$, Table 3; Figure 6). This observation suggests that muscovite content may reflect the degree of isotopic equilibrium. The muscovite in the quartzite mylonite formed either by influx of fluid rich in muscovite constituents or fluid-assisted dissolution-precipitation and neo-crystallized during deformation of RRDSZ (Gottardi & Teyssier, 2013; Gottardi et al., 2011, 2015). The "notch" area has been interpreted to reflect a zone of strain localization (Gottardi & Teyssier, 2013; Gottardi et al., 2015; Methner et al., 2015); therefore, muscovite-rich quartzites collected from that area may have experienced greater recrystallization through a combination of dissolution-reprecipitation and intracrystalline plastic deformation. Strain localization in the notch may have led to enhanced recrystallization and greater isotope exchange in the muscovite-rich quartzites, resulting in greater isotope homogeneity at the scale of isotope measurements and more consistent measured isotope fractionations. Additionally, precipitation of muscovite typically occurs in porous spaces at low stress sites. Therefore, it is possible that the amount of muscovite observed in the notch mylonite reflects to some degree the original porosity of the quartzite before the metamorphic event, that is, high muscovite content correlates with high porosity/permeability and vice versa.

5.3. Fluid-Rock Exchange in the Quartz Veins

Three types of veins were sampled and analyzed in this study: veins cutting through the quartzite mylonite at a high angle to the foliation, low-angle veins, and veins transposed parallel to the foliation (Figure 3). Based on the microstructural record of the veins (Figures 4a–4c), we infer that the low-angle and transposed veins likely originated as high angle veins but were transposed sub-parallel to foliation by progressive shearing. The high-angle quartz veins contain little visible muscovite (Figure 4g), while the low-angle and transposed veins contain large muscovite folia (>250 μm long, up to 100 μm thick, Figures 4h and 4i) oriented sub-parallel to the foliation, suggesting that muscovite grain grew during progressive shearing. The quartz and muscovite $\delta^{18}O$ of low angle and transposed veins ranges from 10.2 to 12.1‰ and 7.5–9.5‰, respectively, which falls within the range of the muscovite-rich quartzite mylonites (Table 3, Figure 6). However, $\delta^{18}O_{ms}$ values in the veins tend to be in the lower range of mylonite $\delta^{18}O_{ms}$ values, with the lowest $\delta^{18}O_{ms}$ value (7.5‰) measured in a transposed vein collected near the bottom of the section (Figure 6). The high angle quartz veins, which lack muscovite, have $\delta^{18}O_{qtz}$ values as low as 9.1‰, the lowest $\delta^{18}O_{qtz}$ value among all quartz samples (Table 3, Figure 6). Therefore, it is reasonable that the high-angle quartz veins encountered the most meteoric water, and the muscovite-poor quartz mylonite came into contact with the least meteoric fluid.

Based on these results, we propose the following model to explain our oxygen and hydrogen stable isotope data sets. During progressive exhumation of the DSZ, high differential stress or increase in strain rate may cause strain hardening and embrittlement, which eventually leads to brittle failure and formation of faults and fractures that allow meteoric fluids to be pumped into the shear zone. During post-rupture relaxation, fractures heal and trap the meteoric fluid in high-angle veins, where isotopic exchange is controlled by bulk crystal diffusion or hydrothermal growth. Deformation and shearing progressively transposed the high angle veins parallel to foliation, and dissolution-precipitation processes led to the growth of muscovite. Dislocation creep processes may cause the fluids to be expelled from the veins into the neighboring quartzite by grain boundary sweeping. However, at this stage the composition of the fluid may have evolved and be less ^{18}O/^{2}H depleted, and therefore not causing much ^{18}O/^{2}H depletion of the quartzite matrix, except in the notch, where high fluid availability is preserved in the abundance of quartz veins present. This process may repeat as an increase in differential stress or accelerating strain rate may cause strain hardening, embrittlement, and eventually brittle failure.

5.4. Fluid-Rock Ratio and Implications for Fluid-Rock Exchange

The isotopic record of DSZ is often difficult to reconcile due to the differences in isotopic exchange kinetics between the different mineral species, which may obscure the isotopic record and affect the degree of equilibrium. This often leads to apparent disequilibrium, especially in DSZ that are being exhumed—or retrograde—where the main driving parameter for isotopic exchange—temperature—is progressively less efficient. Therefore, rather than focusing on each isotopic system and its state of equilibrium, it is often more useful to look at the fluid-rock system as a whole to shed light on the degree of fluid-rock interaction and isotopic equilibrium. We therefore use the approach of Ohmoto and Rye (1974) and Taylor (1978) to investigate our oxygen and hydrogen systems in the context of fluid-rock interaction at different fluid-rock ratios (Figure 8). The hydrogen and oxygen isotope composition of the quartz veins investigated in this study primarily fall within a rock ratio ranging from 0.01 to 0.05, with one vein reaching ~0.1 (Figure 8), suggesting that the fluid-rock exchange was rock-dominated. This result therefore indicates that RRDSZ was not exposed to large volumes of meteoric fluids, which is consistent with the model of meteoric fluid entrapment during brittle episodes discussed in Section 5.3. The muscovite-rich mylonites data set falls almost perfectly in the model using a $\delta^{18}O_{\text{rock-initial}}$ of 12‰ and $\delta^{2}H_{\text{rock-initial}}$ of −65‰, suggesting that these input parameters are valid (Figure 8). The muscovite-rich mylonites showed a spread of low W/R ratio values (0.005–0.05). The muscovite-poor mylonites investigated by Gottardi et al. (2015) are clustered in the 0.01–0.05 range (Figure 8). This could indicate differences in the initial amount of muscovite or different starting conditions for the quartzite mylonite isotopic ratios, as when minerals interact with meteoric fluids, the hydrogen isotopes may be affected by exchange with small volumes of water, while the oxygen does not show meaningful changes in isotopic composition until W/R ratios of >0.05. As the Gottardi et al. (2015) data set display higher $\delta^{18}O_{qtz}$, it likely means that the muscovite-poor quartz mylonite started at a higher $\delta^{18}O_{qtz}$ value compared to the rest of the data.

5.5. Implications for Fluid Flow and Fluid Pathways in Detachment Shear Zones

The high angle veins found within the study area are extensional shear fractures or hybrid shear fractures. These veins are oriented at a high angle to the mylonitic foliation, and two of the three identified sets are perpendicular to the stretching lineation and the transport direction (Figure 3). Although these high angle veins cut through the mylonitic lineation, the quartz fill inside the veins shows evidence of dynamic recrystallization by dislocation creep, suggesting that these veins were deformed at depths where ductile deformation was still active, near the brittle-ductile transition (Figure 4). The presence of these veins at depths equivalent to the seismogenic zone suggests that fluid pressure must have been near-lithostatic or supralithostatic and that deviatoric stress remained low in the footwall of the detachment shear zone (e.g., Reynolds & Lister, 1987; Sibson, 2020). Our stable isotope analyses demonstrate that the fluid present at these depths was meteoric in origin, suggesting that the RRDSZ was permeated by meteoric fluids characterized by low ^{2}H/low ^{18}O as it crossed the brittle-ductile transition (Gottardi et al., 2011, 2015; Methner et al., 2015).

Because the extensional veins formed under high fluid pressure, near-lithostatic or supralithostatic, we suggest that seismic pumping was the most likely mechanism to entrap meteoric fluids at such depths. During evolution of the RRDSZ, an increase in strain rate or stress may have led to strain hardening, embrittlement, and ultimately seismic rupture, causing dilatancy, increase in porosity/permeability, and opening pathways (faults and fractures) used by meteoric fluid to penetrate the DSZ. During post-rupture relaxation, fractures heal and trap the meteoric fluid in high angle veins, where isotopic exchange is controlled by bulk crystal diffusion or hydrothermal growth. The DSZ is still at depth favoring dislocation creep because quartz grains in the vein show evidence of subgrain rotation recrystallization. Under lower stress/slower strain rate, the DSZ returns to condition favoring ductile deformation, and the high angle veins become progressively sheared, transposed, and eventually boudinaged parallel to the foliation. This process may have been repeated several times as the DSZ crossed the brittle-ductile transition.

Fluid flow in large volume of rocks is controlled by permeability, which depends on the interconnectivity of porous spaces (e.g., Putnis, 2021). Crystalline rocks have inherently low permeability; therefore, fluid flow is primarily dependent on fracture permeability and is strongly influenced by the architecture, spacing, and connectivity of the fault zones (Gottardi et al., 2013; Person et al., 2007; Savard et al., 2007). However, in the ductile regime, where rocks can heal and recrystallize, fluid transport remains a conceptually challenging process (e.g., Connolly & Podladchikov, 2004). Recent studies demonstrate that creep-driven porosity can be opened and sustained in rocks at a high-confining pressure during plastic deformation (Dimanov et al., 2007; Fusseis et al., 2009; Gilgannon et al., 2020; Menegon et al., 2015). In order for surface (meteoric) fluids to reach the mid-crustal level where DSZ form, pathways connecting the brittle upper crust to the ductile DSZ must open. Our results suggest that semi-brittle structures such as the veins analyzed in this study may provide such pathways for meteoric fluid to reach mid-crustal depth. Once trapped in the veins, subsequent plastic deformation diffuses the low ^{18}O/low ^{2}H fluid in the surrounding quartzite matrix by processes such as bulk diffusion, crack-assisted diffusion and solute sweeping during grain boundary movement (Kronenberg & Tullis, 1984).

6. Conclusion

In this study, we investigated the stable isotope composition of quartz veins and mylonites from the RRDSZ in order to constrain fluid migration pathways and fluid-rock exchange. Our findings are summarized as follows:

- Hydrogen isotope analyses revealed that the fluid that filled and precipitated in the quartz veins was meteoric in origin. This fluid has a similar composition to the fluid that also permeated the quartzite mylonite.
- Differences in stable isotope depletion correlate with muscovite content. Muscovite forms by dissolution precipitation when nucleation of new grains of muscovite occurs in space between quartz grains. Therefore, the muscovite content may be related to the original porosity of the quartzite mylonite. Samples with the high modal abundance of muscovite and highest porosity displayed the lowest δ^{18}O and δ^{2}H values.
- Fluid-rock ratio depletion modeling suggests that the DSZ was rock-dominated with the highest fluid-rock ratio of ~0.1. We suggest that the fluid entered the system episodically through semi-brittle structures (veins) and was subsequently expelled out and into the surrounding mylonite with progressive shearing.
- Our results suggest that veins provided pathways for meteoric fluids to enter the shear zone, and that stable isotope depletion patterns follow fluid availability and porosity of the mylonite.

Data Availability Statement

The data presented in this publication is available on EarthChem (Gottardi & Mire, 2024).

Acknowledgments
This work was supported by the National Science Foundation Grant EAR-1849812 to RG and GC. We thank J. Cullen for help with stable isotope analyses. We gratefully acknowledge G-Cubed Editor Whitney Behr, and detailed reviews by Chloe Bonamici and an anonymous reviewer that greatly improved this manuscript.

References

Armstrong, R. L. (1968). Mantled gneiss domes in the Albion Range, southern Idaho. *Geological Society of America Bulletin*, *79*(10), 1295–1314. https://doi.org/10.1130/0016-7606(1968)79[1295:mgdita]2.0.co;2

Armstrong, R. L., & Hills, F. A. (1967). Rubidiumstrontium and potassium argon geochronologic studies of mantled gneiss domes, Albion Range, southern Idaho, USA. *Earth and Planetary Science Letters*, *3*(11), 114–124. https://doi.org/10.1016/0012-821x(67)90021-0

Axen, G. J. (1992). Pore pressure, stress increase, and fault weakening in low-angle normal faulting. *Journal of Geophysical Research*, *97*(B6), 8979–8991. https://doi.org/10.1029/92JB00517

Baumgartner, L. P., & Valley, J. W. (2001). Stable isotope transport and contact metamorphic fluid flow. *Reviews in Mineralogy and Geochemistry*, *43*(1), 415–467. https://doi.org/10.2138/gsrmg.43.1.415

Behr, W. M., & Platt, J. P. (2014). Brittle faults are weak, yet the ductile middle crust is strong: Implications for lithospheric mechanics. *Geophysical Research Letters*, *41*(22), 8067–8075. https://doi.org/10.1002/2014gl061349

Bons, P. D., & Gomez-Rivas, E. (2020). Origin of meteoric fluids in extensional detachments. *Geofluids*, *2020*, 1–8. https://doi.org/10.1155/2020/7201545

Brace, W. F., & Kohlstedt, D. L. (1980). Limits on lithospheric stress imposed by laboratory experiments. *Journal of Geophysical Research*, *85*(B11), 6248–6252. https://doi.org/10.1029/JB085iB11p06248

Byerlee, J. (1978). Friction of rocks. *Rock Friction and Earthquake Prediction*, 615–626. https://doi.org/10.1007/978-3-0348-7182-2_4

Carter, N. L., Kronenberg, A. K., Ross, J. V., & Wiltschko, D. V. (1990). Control of fluids on deformation of rocks. *Geological Society, London, Special Publications*, *54*(1), 1–13. https://doi.org/10.1144/gsl.sp.1990.054.01.01

Chacko, T., Hu, X., Mayeda, T. K., Clayton, R. N., & Goldsmith, J. R. (1996). Oxygen isotope fractionations in muscovite, phlogopite, and rutile. *Geochimica et Cosmochimica Acta*, *60*(14), 2595–2608. https://doi.org/10.1016/0016-7037(96)00112-3

Compton, R. R. (1975). Geologic map of the Park Valley quadrangle, Box Elder County, Utah, and Cassia County, Idaho. (873).

Compton, R. R. (1980). Fabrics and strains in quartzites of a metamorphic core complex, Raft River Mountains, Utah.

Compton, R. R., Todd, V. R., Zartman, R. E., & Naeser, C. W. (1977). Oligocene and Miocene metamorphism, folding, and low-angle faulting in northwestern Utah. *Geological Society of America Bulletin*, *88*(9), 1237–1250. https://doi.org/10.1130/0016-7606(1977)88%3C1237:OAMMFA%3E2.0.CO;2

Connolly, J. A., & Podladchikov, Y. Y. (2004). Fluid flow in compressive tectonic settings: Implications for midcrustal seismic reflectors and downward fluid migration. *Journal of Geophysical Research*, *109*(B4), B04201. https://doi.org/10.1029/2003JB002822

Dimanov, A., Rybacki, E., Wirth, R., & Dresen, G. (2007). Creep and strain-dependent microstructures of synthetic anorthite–diopside aggregates. *Journal of Structural Geology*, *29*(6), 1049–1069. https://doi.org/10.1016/j.jsg.2007.02.010

Dusséaux, C., Gébelin, A., Boulvais, P., Ruffet, G., Poujol, M., Cogné, N., et al. (2022). Timing and duration of meteoric water infiltration in the Quiberon detachment zone (Armorican Massif, Variscan belt, France). *Journal of Structural Geology*, *156*, 104546. https://doi.org/10.1016/j.jsg.2022.104546

Ferry, J. M. (1994). A historical review of metamorphic fluid flow. *Journal of Geophysical Research*, *99*(B8), 15487–15498. https://doi.org/10.1029/94jb01147

Fricke, H. C., Wickham, S. M., & O'Neil, J. R. (1992). Oxygen and hydrogen isotope evidence for meteoric water infiltration during mylonitization and uplift in the Ruby Mountains-East Humboldt Range core complex, Nevada. *Contributions to Mineralogy and Petrology*, *111*(2), 203–221. https://doi.org/10.1007/BF00348952

Fusseis, F., Regenauer-Lieb, K., Liu, J., Hough, R. M., & De Carlo, F. (2009). Creep cavitation can establish a dynamic granular fluid pump in ductile shear zones. *Nature*, *459*(7249), 974–977. https://doi.org/10.1038/nature08051

Gébelin, A., Mulch, A., Teyssier, C., Chamberlain, C. P., & Heizler, M. (2012). Coupled basin-detachment systems as paleoaltimetry archives of the western North American Cordillera. *Earth and Planetary Science Letters*, *335*, 36–47. https://doi.org/10.1016/j.epsl.2012.04.029

Gébelin, A., Mulch, A., Teyssier, C., Heizler, M., Vennemann, T., & Seaton, N. C. (2011). Oligo-Miocene extensional tectonics and fluid flow across the Northern Snake Range detachment system, Nevada. *Tectonics*, *30*(5). https://doi.org/10.1029/2010TC002797

Gébelin, A., Mulch, A., Teyssier, C., Jessup, M. J., Law, R. D., & Brunel, M. (2013). The Miocene elevation of Mount Everest. *Geology*, *41*(7), 799–802. https://doi.org/10.1130/G34331.1

Gébelin, A., Teyssier, C., Heizler, M. T., & Mulch, A. (2015). Meteoric water circulation in a rolling-hinge detachment system (northern Snake Range core complex, Nevada). *Bulletin*, *127*(1–2), 149–161. https://doi.org/10.1130/B31063.1

Gilgannon, J., Poulet, T., Berger, A., Barnhoorn, A., & Herwegh, M. (2020). Dynamic recrystallization can produce porosity in shear zones. *Geophysical Research Letters*, *47*(7), e2019GL086172. https://doi.org/10.1029/2019gl086172

Gottardi, R., & Hughes, B. (2022). Role of fluids on deformation in mid-crustal shear zones, Raft River Mountains, Utah. *Geological Magazine*, *159*(11–12), 2206–2218. https://doi.org/10.1017/s0016756822000231

Gottardi, R., Kao, P.-H., Saar, M. O., & Teyssier, C. (2013). Effects of permeability fields on fluid, heat, and oxygen isotope transport in extensional detachment systems. *Geochemistry, Geophysics, Geosystems*, *14*(5), 1493–1522. https://doi.org/10.1002/ggge.20100

Gottardi, R., & Mire, C. (2024). Oxygen and hydrogen stable isotope data from the Raft River metamorphic core complex (Utah, USA), version 1.0 [Dataset]. *Interdisciplinary Earth Data Alliance (IEDA)*. https://doi.org/10.60520/IEDA/113175

Gottardi, R., Schaper, M. C., Barnes, J. D., & Heizler, M. T. (2018). Fluid–rock interaction and strain localization in the picacho mountains detachment shear zone, Arizona, USA. *Tectonics*, *37*(9), 3244–3260. https://doi.org/10.1029/2017TC004835

Gottardi, R., & Teyssier, C. (2013). Thermomechanics of an extensional shear zone, Raft River metamorphic core complex, NW Utah. *Journal of Structural Geology*, *53*, 54–69. https://doi.org/10.1016/j.jsg.2013.05.012

Gottardi, R., Teyssier, C., Mulch, A., Valley, J. W., Spicuzza, M. J., Vennemann, T. W., et al. (2015). Strain and permeability gradients traced by stable isotope exchange in the Raft River detachment shear zone, Utah. *Journal of Structural Geology*, *71*, 41–57. https://doi.org/10.1016/j.jsg.2014.10.005

Gottardi, R., Teyssier, C., Mulch, A., Vennemann, T. W., & Wells, M. L. (2011). Preservation of an extreme transient geotherm in the Raft River detachment shear zone. *Geology*, *39*(8), 759–762. https://doi.org/10.1130/G31834.1

Gratier, J. P., Dysthe, D. K., & Renard, F. (2013). The role of pressure solution creep in the ductility of the Earth's upper crust. *Advances in Geophysics*, *54*, 47–179. https://doi.org/10.1016/b978-0-12-380940-7.00002-0

Griggs, D. (1967). Hydrolytic weakening of quartz and other silicates. *Geophysical Journal International*, *14*(1–4), 19–31. https://doi.org/10.1111/j.1365-246x.1967.tb06218.x

Hobbs, B. E., Ord, A., Spalla, M. I., Gosso, G., & Zucali, M. (2010). The interaction of deformation and metamorphic reactions. *Geological Society, London, Special Publications*, *332*(1), 189–223. https://doi.org/10.1144/sp332.12

Ingebritsen, S. E., & Manning, C. E. (2010). Permeability of the continental crust: Dynamic variations inferred from seismicity and metamorphism. *Geofluids*, *10*(1-2), 193–205. https://doi.org/10.1111/j.1468-8123.2010.00278.x

Kerrich, R., & Rehrig, W. (1987). Fluid motion associated with Tertiary mylonitization and detachment faulting: $^{18}O/^{16}O$ evidence from the Picacho metamorphic core complex, Arizona. *Geology*, *15*(1), 58–62. https://doi.org/10.1130/0091-7613(1987)15%3C58:FMAWTM%3E2.0.CO;2

Kronenberg, A. K., & Tullis, J. (1984). Flow strengths of quartz aggregates: Grain size and pressure effects due to hydrolytic weakening. *Journal of Geophysical Research*, *89*(B6), 4281–4297. https://doi.org/10.1029/jb089ib06p04281

Kusznir, N. J., & Park, R. G. (1987). The extensional strength of the continental lithosphere: Its dependence on geothermal gradient, and crustal composition and thickness. *Geological Society, London, Special Publications*, *28*(1), 35–52. https://doi.org/10.1144/GSL.SP.1987.028.01.04

Labrousse, L., Hetényi, G., Raimbourg, H., Jolivet, L., & Andersen, T. B. (2010). Initiation of crustal-scale thrusts triggered by metamorphic reactions at depth: Insights from a comparison between the Himalayas and Scandinavian Caledonides. *Tectonics*, *29*(5). https://doi.org/10.1029/2009tc002602

Lister, G. S., & Snoke, A. W. (1984). SC mylonites. *Journal of Structural Geology*, *6*(6), 617–638. https://doi.org/10.1016/0191-8141(84)90001-4

Malavieille, J. (1987). Extensional shearing deformation and kilometer-scale "a"-type folds in a Cordilleran Metamorphic Core Complex (Raft River Mountains, northwestern Utah). *Tectonics*, *6*(4), 423–448. https://doi.org/10.1029/TC006i004p00423

McCaig, A. M. (1988). Deep fluid circulation in fault zones. *Geology*, *16*(10), 867–870. https://doi.org/10.1130/0091-7613(1988)016<0867:dfcifz>2.3.co;2

Menegon, L., Fusseis, F., Stünitz, H., & Xiao, X. (2015). Creep cavitation bands control porosity and fluid flow in lower crustal shear zones. *Geology*, *43*(3), 227–230. https://doi.org/10.1130/g36307.1

Methner, K., Mulch, A., Teyssier, C., Wells, M. L., Cosca, M. A., Gottardi, R., et al. (2015). Eocene and Miocene extension, meteoric fluid infiltration, and core complex formation in the Great Basin (Raft River Mountains, Utah). *Tectonics*, *34*(4), 680–693. https://doi.org/10.1002/2014TC003766

Morrison, J. (1994). Meteoric water-rock interaction in the lower plate of the Whipple Mountain metamorphic core complex, California. *Journal of Metamorphic Geology*, *12*(6), 827–840. https://doi.org/10.1111/j.1525-1314.1994.tb00062.x

Morrison, J., & Anderson, J. L. (1998). Footwall refrigeration along a detachment fault: Implications for the thermal evolution of core complexes. *Science*, *279*(5347), 63–66. https://doi.org/10.1126/science.279.5347.63

Mulch, A., Cosca, M. A., Andresen, A., & Fiebig, J. (2005). Time scales of deformation and exhumation in extensional detachment systems determined by high-spatial resolution in situ UV-laser ^{40}Ar/^{39}Ar dating. *Earth and Planetary Science Letters*, *233*(3–4), 375–390. https://doi.org/10.1016/j.epsl.2005.01.042

Mulch, A., Teyssier, C., Cosca, M. A., & Chamberlain, C. P. (2007). Stable isotope paleoaltimetry of Eocene core complexes in the North American Cordillera. *Tectonics*, *26*(4). https://doi.org/10.1029/2006TC001995

Mulch, A., Teyssier, C., Cosca, M. A., Vanderhaeghe, O., & Vennemann, T. W. (2004). Reconstructing paleoelevation in eroded orogens. *Geology*, *32*(6), 525–528. https://doi.org/10.1130/G20394.1

Mulch, A., Teyssier, C., Cosca, M. A., & Vennemann, T. W. (2006). Thermomechanical analysis of strain localization in a ductile detachment zone. *Journal of Geophysical Research*, *111*(B12), B12405. https://doi.org/10.1029/2005jb004032

Ohmoto, H., & Rye, R. O. (1974). Hydrogen and oxygen isotopic compositions of fluid inclusions in the Kuroko deposits, Japan. *Economic Geology*, *69*(6), 947–953. https://doi.org/10.2113/gsecongeo.69.6.947

Okazaki, K., Burdette, E., & Hirth, G. (2021). Rheology of the fluid oversaturated fault zones at the brittle-plastic transition. *Journal of Geophysical Research: Solid Earth*, *126*(2), e2020JB020804. https://doi.org/10.1029/2020jb020804

Person, M., Mulch, A., Teyssier, C., & Gao, Y. (2007). Isotope transport and exchange within metamorphic core complexes. *American Journal of Science*, *307*(3), 555–589. https://doi.org/10.2475/03.2007.01

Pongrac, P., Jeřábek, P., Stünitz, H., Raimbourg, H., Heilbronner, R., Racek, M., & Nègre, L. (2022). Mechanical properties and recrystallization of quartz in presence of H_2O: Combination of cracking, subgrain rotation and dissolution-precipitation processes. *Journal of Structural Geology*, *160*, 104630. https://doi.org/10.1016/j.jsg.2022.104630

Putnis, A. (2021). Fluid–mineral interactions: Controlling coupled mechanisms of reaction, mass transfer and deformation. *Journal of Petrology*, *62*(12). https://doi.org/10.1093/petrology/egab092

Quilichini, A., Siebenaller, L., Nachlas, W. O., Teyssier, C., Vennemann, T. W., Heizler, M. T., & Mulch, A. (2015). Infiltration of meteoric fluids in an extensional detachment shear zone (Kettle dome, WA, USA): How quartz dynamic recrystallization relates to fluid-rock interaction. *Journal of Structural Geology*, *71*, 71–85. https://doi.org/10.1016/j.jsg.2014.11.008

Quilichini, A., Siebenaller, L., Teyssier, C., & Vennemann, T. W. (2016). Magmatic and meteoric fluid flow in the Bitterroot extensional detachment shear zone (MT, USA) from ductile to brittle conditions. *Journal of Geodynamics*, *101*, 109–128. https://doi.org/10.1016/j.jog.2016.05.006

Reynolds, S. J., & Lister, G. S. (1987). Structural aspects of fluid-rock interactions in detachment zones. *Geology*, *15*(4), 362–366. https://doi.org/10.1130/0091-7613(1987)15%3C362:SAOFII%3E2.0.CO;2

Roddy, M. S., Reynolds, S. J., Smith, B. M., & Ruiz, J. (1988). K-metasomatism and detachment-related mineralization, Harcuvar Mountains, Arizona. *Geological Society of America Bulletin*, *100*(10), 1627–1639. https://doi.org/10.1130/0016-7606(1988)100%3C1627:KMADRM%3E2.3.CO;2

Saar, M. O., & Manga, M. (2004). Depth dependence of permeability in the Oregon Cascades inferred from hydrogeologic, thermal, seismic, and magmatic modeling constraints. *Journal of Geophysical Research*, *109*(B4), B04204. https://doi.org/10.1029/2003jb002855

Saltzer, S. D., & Hodges, K. V. (1988). The Middle Mountain shear zone, southern Idaho: Kinematic analysis of an early Tertiary high-temperature detachment. *Geological Society of America Bulletin*, *100*(1), 96–103. https://doi.org/10.1130/0016-7606(1988)100%3C0096:TMMSZS%3E2.3.CO;2

Savard, C., Beaudoin, G., & Therrien, R. (2007). Numerical modelling of 3D fluid flow and oxygen isotope exchange in fractured media: Spatial distribution of isotope patterns. *Geofluids*, *7*(4), 387–400. https://doi.org/10.1111/j.1468-8123.2007.00193.x

Sharp, Z. D. (1990). A laser-based microanalytical method for the in situ determination of oxygen isotope ratios of silicates and oxides. *Geochimica et Cosmochimica Acta*, *54*(5), 1353–1357. https://doi.org/10.1016/0016-7037(90)90160-M

Sharp, Z. D., Atudorei, V., & Durakiewicz, T. (2001). A rapid method for determination of hydrogen and oxygen isotope ratios from water and hydrous minerals. *Chemical Geology*, *178*(1–4), 197–210. https://doi.org/10.1016/S0009-2541(01)00262-5

Sharp, Z. D., & Kirschner, D. L. (1994). Quartz-calcite oxygen isotope thermometry: A calibration based on natural isotopic variations. *Geochimica et Cosmochimica Acta*, *58*(20), 4491–4501. https://doi.org/10.1016/0016-7037(94)90350-6

Shimizu, I. (1995). Kinetics of pressure solution creep in quartz: Theoretical considerations. *Tectonophysics*, *245*(3–4), 121–134. https://doi.org/10.1016/0040-1951(94)00230-7

Sibson, R. H. (1990). Conditions for fault-valve behaviour. *Geological Society, London, Special Publications*, *54*(1), 15–28. https://doi.org/10.1144/gsl.sp.1990.054.01.02

Sibson, R. H. (1992). Implications of fault-valve behaviour for rupture nucleation and recurrence. *Tectonophysics*, *211*(1–4), 283–293. https://doi.org/10.1016/0040-1951(92)90065-E

Sibson, R. H. (2020). Preparation zones for large crustal earthquakes consequent on fault-valve action. *Earth Planets and Space*, *72*, 1–20. https://doi.org/10.1186/s40623-020-01153-x

Smith, B. M., Reynolds, S. J., Day, H. W., & Bodnar, R. J. (1991). Deep-seated fluid involvement in ductile-brittle deformation and mineralization, South Mountains metamorphic core complex, Arizona. *Geological Society of America Bulletin*, *103*(4), 559–569. https://doi.org/10.1130/0016-7606(1991)103%3C0559:DSFIID%3E2.3.CO;2

Spencer, J. E., & Welty, J. W. (1986). Possible controls of base-and precious-metal mineralization associated with Tertiary detachment faults in the lower Colorado River trough, Arizona and California. *Geology*, *14*(3), 195–198. https://doi.org/10.1130/0091-7613(1986)14%3C195:PCOBAP%3E2.0.CO;2

Spruzeniece, L., & Piazolo, S. (2015). Strain localization in brittle–ductile shear zones: Fluid-abundant vs. fluid-limited conditions (an example from Wyangala area, Australia). *Solid Earth*, *6*(3), 881–901. https://doi.org/10.5194/se-6-881-2015

Stenvall, C. A., Fagereng, A., Diener, J. F. A., Harris, C., & Janney, P. E. (2020). Sources and effects of fluids in continental retrograde shear zones: Insights from the Kuckaus Mylonite Zone, Namibia. *Geofluids*, *2020*, 1–21. https://doi.org/10.1155/2020/3023268

Stünitz, H., Thust, A., Heilbronner, R., Behrens, H., Kilian, R., Tarantola, A., & Fitz Gerald, J. D. (2017). Water redistribution in experimentally deformed natural milky quartz single crystals—Implications for H_2O-weakening processes. *Journal of Geophysical Research: Solid Earth*, *122*(2), 866–894. https://doi.org/10.1002/2016jb013533

Sullivan, W. A. (2008). Significance of transport-parallel strain variations in part of the Raft River shear zone, Raft River Mountains, Utah, USA. *Journal of Structural Geology*, *30*(2), 138–158. https://doi.org/10.1016/j.jsg.2007.11.007

Suzuoki, T., & Epstein, S. (1976). Hydrogen isotope fractionation between OH-bearing minerals and water. *Geochimica et Cosmochimica Acta*, *40*(10), 1229–1240. https://doi.org/10.1016/0016-7037(76)90158-7

Taylor, H. P., Jr. (1978). Oxygen and hydrogen isotope studies of plutonic granitic rocks. *Earth and Planetary Science Letters*, *38*(1), 177–210. https://doi.org/10.1016/0012-821x(78)90131-0

Valley, J. W. (2001). Stable isotope thermometry at high temperatures. *Reviews in Mineralogy and Geochemistry*, *43*(1), 365–413. https://doi.org/10.2138/gsrmg.43.1.365

Valley, J. W., Kitchen, N., Kohn, M. J., Niendorf, C. R., & Spicuzza, M. J. (1995). UWG-2, a garnet standard for oxygen isotope ratios: Strategies for high precision and accuracy with laser heating. *Geochimica et Cosmochimica Acta*, *59*(24), 5223–5231. https://doi.org/10.1016/0016-7037(95)00386-X

Vollmer, F. W. (2015). Orient 3: A new integrated software program for orientation data analysis, kinematic analysis, spherical projections, and Schmidt plots. *Geological Society of America Abstracts with Programs*, *47*(7), 49.

Vollmer, F. W. (2023). Orient: Directional data analysis software. https://vollmerf.github.io/orient/

Wassmann, S., & Stőckhert, B. (2013). Rheology of plate interface—Dissolution precipitation creep in high pressure metamorphic rocks. *Tectonophysics*, *608*, 1–29. https://doi.org/10.1016/j.tecto.2013.09.030

Wehrens, P., Berger, A., Peters, M., Spillmann, T., & Herwegh, M. (2016). Deformation at the frictional-viscous transition: Evidence for cycles of fluid-assisted embrittlement and ductile deformation in the granitoid crust. *Tectonophysics*, *693*, 66–84. https://doi.org/10.1016/j.tecto.2016.10.022

Wells, M. L. (1997). Alternating contraction and extension in the hinterlands of orogenic belts: An example from the Raft River Mountains, Utah. *Geological Society of America Bulletin*, *109*(1), 107–126. https://doi.org/10.1130/0016-7606(1997)109<0107:acaeit>2.3.co;2

Wells, M. L. (2001). Rheological control on the initial geometry of the Raft River detachment fault and shear zone, western United States. *Tectonics*, *20*(4), 435–457. https://doi.org/10.1029/2000TC001202

Wells, M. L., Hoisch, T. D., Peters, M. T., Miller, D. M., Wolff, E. D., & Hanson, L. M. (1998). The Mahogany Peaks fault, a Late Cretaceous-Paleocene (?) normal fault in the hinterland of the Sevier orogen. *The Journal of Geology*, *106*(5), 623–634. https://doi.org/10.1086/516046

Wells, M. L., Snee, L. W., & Blythe, A. E. (2000). Dating of major normal fault systems using thermochronology: An example from the Raft River detachment, Basin and Range, western United States. *Journal of Geophysical Research*, *105*(B7), 16303–16327. https://doi.org/10.1029/2000jb900094

Whyte, A. J., Weller, O. M., Copley, A. C., & St-Onge, M. R. (2021). Quantifying water diffusivity and metamorphic reaction rates within mountain belts, and their implications for the rheology of cratons. *Geochemistry, Geophysics, Geosystems*, *22*(11), e2021GC009988. https://doi.org/10.1029/2021gc009988

Wickham, S. M., & Taylor, H. P. (1987). Stable isotope constraints on the origin and depth of penetration of hydrothermal fluids associated with Hercynian regional metamorphism and crustal anatexis in the Pyrenees. *Contributions to Mineralogy and Petrology*, *95*(3), 255–268. https://doi.org/10.1007/BF00371841